REPORT DOCUMENTATION PAGE

The public reporting burden for this collection of information is estimated to average 1 hour per response, including the time for reviewing instructions, searching existing data sources, gathering and maintaining the data needed, and completing and reviewing the collection of information. Send comments regarding this burden estimate or any other aspect of this collection of information, including suggestions for reducing the burden, to Department of Defense, Washington Headquarters Services, Directorate for Information Operations and Reports (0704-0188), 1215 Jefferson Davis Highway, Suite 1204, Arlington, VA 22202-4302. Respondents should be aware that notwithstanding any other provision of law, no person shall be subject to any penalty for failing to comply with a collection of information if it does not display a currently valid OMB control number.
PLEASE DO NOT RETURN YOUR FORM TO THE ABOVE ADDRESS.

1. REPORT DATE (DD-MM-YYYY)	2. REPORT TYPE	3. DATES COVERED (From - To)
06/30/2002	Final	7/1/2000 - 6/30/2002

4. TITLE AND SUBTITLE

Development of a Computer Aided Weld Design Tool

5a. CONTRACT NUMBER

5b. GRANT NUMBER

N00014-00-1-0741

5c. PROGRAM ELEMENT NUMBER

6. AUTHOR(S)

Panagiotis Michaleris

5d. PROJECT NUMBER

00PR07429

5e. TASK NUMBER

5f. WORK UNIT NUMBER

7. PERFORMING ORGANIZATION NAME(S) AND ADDRESS(ES)

The Pennsylvania State University
110 Technology Center, 200 Innovation Blvd.
University Park, PA 16802

8. PERFORMING ORGANIZATION REPORT NUMBER

9. SPONSORING/MONITORING AGENCY NAME(S) AND ADDRESS(ES)

Office of Naval Research
Ballston Centre Tower One
800 North Quincy Street
Arlington, VA 22217-5660

10. SPONSOR/MONITOR'S ACRONYM(S)

11. SPONSOR/MONITOR'S REPORT NUMBER(S)

12. DISTRIBUTION/AVAILABILITY STATEMENT

Approved for Public Release; Distribution is Unlimited

13. SUPPLEMENTARY NOTES

14. ABSTRACT

Contributed to the development of a Lagrangial thermo-mechanical process optimization approach. The methodology was demonstrated in the optimization of the thermal tensioning process for the minimization of welding residual stress elimination of buckling distortion.

Developed eigenvalue sensitivity analysis capabilities for the prediction and elimination of buckling distortion in large welded structures.

Initiated research on the coupled multi-scale therm-mechanical process modeling of large structures. The approach combines adaptivity and domain decomposition for both temporal and spatial multi-scale problems.

15. SUBJECT TERMS

16. SECURITY CLASSIFICATION OF:			17. LIMITATION OF ABSTRACT	18. NUMBER OF PAGES	19a. NAME OF RESPONSIBLE PERSON
a. REPORT	b. ABSTRACT	c. THIS PAGE			Robert Killoren
				73	19b. TELEPHONE NUMBER (Include area code)
					814-865-1372

1118 094

FINAL REPORT
TO OFFICE OF NAVAL RESEARCH

"Development of a Computer Aided Weld Design Tool"

N00014-00-1-0741

March 2003

Dr. Panagiotis Michaleris
Department of Mechanical and Nuclear Engineering
The Pennsylvania State University

Contract Information

Contract Number	N000140010741
Title of Research	Development of a Computer Aided Weld Design Tool
Principal Investigator	Panagiotis (Pan) Michaleris
Organization	The Pennsylvania State University

Technical Section

0.1 Technical Objectives

The objective of this project is to develop a computer aided weld design tool for a computer integrated design and manufacturing system.

The weld design tool will allow for the determination of appropriate welding conditions and if needed auxiliary heating for a specific structural design such that welding distortion is within tolerance. The database will be integrated with Computer Aided Production Engineering (CAPE) software.

The project contributes to a collaborative effort by Maglev Inc and other Universities entitled "Demonstration of Computer Aided Manufactuting Techniques for the Precision Fabrication of Large Steel Curved Plate Beam Components for Shipbuilding and Other Industries."

0.2 Technical Approach

The proposed program is organized in the following five tasks:

1. Identification of structural features that welding distortion
2. Inverse method and database architecture
3. Generation of a database
4. Integration with computer aided production engineering software
5. Modifications and refinement using production tests

0.3 Progress

Progress was achieved in the following topics:

- Contributed to the development of a Lagrangial thermo-mechanical process optimization approach. The methodology was demonstrated in the optimization of the thermal tensioning process for the minimization of welding residual stress elimination of buckling distortion.
- Developed eigenvalue and large deformation sensitivity analysis capabilities for the prediction of buckling distortion and bowing distortion in large welded structures.
- Initiated research on the coupled multi-scale therm-mechanical process modeling of large structures. The approach combines adaptivity and domain decomposition for both temporal and spatial multi-scale problems.

Chapter 1

Sensitivity Analysis and Optimization of Thermo-Elasto-Plastic Processes [1]

---

[1]The work presented in this chapter has been submitted for review to *Computer Methods in Applied Mechanics and Engineering*

1.1 Introduction

1.2 Analytical Formulation

Finite element formulations for quasi-static thermo-elasto-plastic processes in Lagrangian reference frames have been widely used [1, 2, 3, 4, 5, 6, 7, 8, 9]. The thermal analysis is assumed to be transient while the elasto-plastic quasi-static. Thermo-elasto-plastic processes are typically assumed to be weakly coupled, that is, the temperature profile is assumed to be independent of stresses and strains. Thus a heat transfer analysis is performed initially, and the results are imported for the mechanical analysis.

1.2.1 Transient Thermal Analysis

For a spatial frame $\mathbf{x}$ fixed to the body, and time t, the governing equation for transient heat conduction analysis is given by the following:

$$\rho C_p \frac{dT}{dt} = \nabla \cdot [\mathbf{k} \nabla T] + Q \qquad \text{in the entire volume } V \text{ of the material} \qquad (1.1)$$

where ρ is the density of the flowing body, C_p is the specific heat capacity, T is the temperature, $\mathbf{k}$ is the temperature-dependent thermal conductivity matrix, Q is the internal heat generation rate and ∇ is the spatial gradient operator.

The initial temperature field is given by

$$T = T^0 \qquad \text{in the entire volume } V \qquad (1.2)$$

where T^0 is the prescribed initial temperature. The following boundary conditions are applied on the surface:

$$
\begin{aligned}
T &= \bar{T} && \text{on the surface } A^T \text{, with prescribed temperatures } \bar{T} & (1.3) \\
q &= \bar{q} && \text{on the surface } A^q \text{, with prescribed heat fluxes } \bar{q} & (1.4)
\end{aligned}
$$

Through the finite element formulation, the element residual vector $\mathbf{R}$ is obtained as follows

$$
\begin{aligned}
\mathbf{R}(^n\mathbf{T}) &= \sum_V \left\{ \mathbf{B}^T \mathbf{k} \mathbf{B} \, ^n\mathbf{T} - \mathbf{N}^T Q + \mathbf{N}^T \mathbf{N} \rho C_p \frac{^n\mathbf{T} - \, ^{n-1}\mathbf{T}}{^nt - \, ^{n-1}t} \right\} W J \\
&\quad + \sum_{A_q} \mathbf{N}^T \bar{q} w j
\end{aligned}
\qquad (1.5)
$$

where left superscripts $n-1$ and n represent the time increments ^{n-1}t and ^nt, $\mathbf{T}$ is element nodal temperature vector, $\mathbf{N}$ and $\mathbf{B}$ are the usual matrices which interpolate the temperature T and temperature gradient ∇T in an element; J and j are the volume and area Jacobian component corresponding to the Gaussian weighting W for volume and w for surface integration. The Global residual vector $\mathcal{R}$ is assembled from the element residual vector as follows

$$\mathcal{R}(^n\mathcal{T}) = \sum_{Elements} \mathbf{R}(^n\mathbf{T}) = 0 \qquad (1.6)$$

where $\mathcal{T}$ is the global temperature vector. Equation (1.6) is solved in an incremental iterative fashion.

1.2.2 Mechanical Analysis

$$\nabla \cdot \mathbf{S} + \mathbf{b} = 0 \qquad \text{in } V \tag{1.7}$$

where $\mathbf{S}$ is the second-order stress tensor, and $\mathbf{b}$ the body force vector. The boundary conditions are:

$$\begin{aligned} \mathbf{u} &= \bar{\mathbf{u}} & \text{on surface } A^u \tag{1.8} \\ \mathbf{Sn} &= \bar{\mathbf{t}} & \text{on surface } A^t \tag{1.9} \end{aligned}$$

where $\bar{\mathbf{u}}$ are the prescribed displacements on surface A^u, $\bar{\mathbf{t}}$ are the prescribed tractions on surface A^t, and $\mathbf{n}$ is the unit outward normal to the surface A^t. The total strain is the Green's strain:

$$\mathbf{E} = \frac{1}{2}\left\{\nabla \mathbf{u} + [\nabla \mathbf{u}]^T\right\} \tag{1.10}$$

Thanks for the symmetry, the stress tensor $\mathbf{S}$ and strain tensor $\mathbf{E}$ are commonly expressed in the vector form σ and ϵ (usually called engineering stress and strain) for the computational efficiency. Then the initial conditions are:

$$\begin{aligned} \mathbf{u} &= \mathbf{u}^0 \tag{1.11} \\ \epsilon_p &= \epsilon_p{}^0 \tag{1.12} \\ \epsilon_q &= \epsilon_q{}^0 \tag{1.13} \end{aligned}$$

where ϵ_p is the plastic strain vector and ϵ_q is the equivalent plastic strain.

Assuming small deformation thermo-elasto-plasticity, the total strain vector ϵ is decomposed into the elastic strain vector ϵ_e, ϵ_p and thermal strain vector ϵ_t:

$$\epsilon = \epsilon_e + \epsilon_p + \epsilon_t \tag{1.14}$$

The stress strain relationship is:

$$\sigma = \mathbf{C}\epsilon_e = \mathbf{C}\left[\epsilon - \epsilon_p - \epsilon_t\right] \tag{1.15}$$

where $\mathbf{C}$ is the temperature-dependent material stiffness tensor.

Through the finite element formulations, the element residual $\mathbf{R}$ is obtained as follows

$$\mathbf{R}(^n\mathbf{U}) = \sum_V \left[\mathbf{B}^T{}^n\sigma - \mathbf{N}^T\mathbf{b}\right] WJ - \sum_{A^t} \mathbf{N}^T\bar{\mathbf{t}}wj \tag{1.16}$$

where

$$^n\sigma = {}^{n-1}\sigma + \Delta\sigma \tag{1.17}$$

Differentiating equation (1.15) using incremental expression yields following equations

$$\Delta\sigma = {}^n\mathbf{C}\left[\Delta\epsilon - \Delta\epsilon_p - \Delta\epsilon_t\right] + \Delta\mathbf{C}\,{}^{n-1}\epsilon_e \tag{1.18}$$

The elastic predictor σ_B and corresponding elastic strain ϵ_{Be} are defined as follows

$$\begin{aligned} \sigma_B &= {}^{n-1}\sigma + {}^n\mathbf{C}\left[\Delta\epsilon - \Delta\epsilon_t\right] + \Delta\mathbf{C}\,{}^{n-1}\epsilon_e \tag{1.19} \\ \epsilon_{Be} &= {}^{n-1}\epsilon_e + \left[\Delta\epsilon - \Delta\epsilon_t\right] \tag{1.20} \end{aligned}$$

Using the associative J_2 plasticity [10], the yield function f is:

$$f = \sigma_m - \sigma_Y \tag{1.21}$$

where σ_m and σ_Y are the Mises stress and yield stress. Active yielding occurs when $f \geq 0$. In case of active yielding, the evolution of $\Delta\epsilon_q$ can be evaluated by the radial return algorithm [1].

$$\Delta\epsilon_p = \Delta\epsilon_q \mathbf{a} \tag{1.22}$$

where

$$\mathbf{a} = \frac{3}{2}\mathbf{Lm} \tag{1.23}$$

$$\mathbf{m} = \frac{1}{\sigma_{Bm}}\mathbf{s}_B \tag{1.24}$$

$$\mathbf{L} = diag(\begin{array}{cccccc} 1 & 1 & 1 & 2 & 2 & 2 \end{array}) \tag{1.25}$$

where σ_{Bm} and $\mathbf{s}_B$ are the Mises stress and the deviatoric stress of the elastic predictor σ_B.

1.3 Sensitivity Analysis from the Method of Direct Differentiation

1.3.1 Thermal Sensitivity

Differentiating Equation (1.6) with respect to each of the design variable ϕ_i yields:

$$\frac{d^n\mathcal{T}}{d\phi_i} = -\left\{\left[\frac{d\mathcal{R}}{d^n\mathcal{T}}\right]^{-1}_{constant\ \phi_i}\right\}\frac{\mathcal{D}\mathcal{R}}{\mathcal{D}\phi_i} \tag{1.26}$$

where $\mathcal{D}$ stands for the contribution due to all variables except for $\mathcal{T}$. Because the global stiffness has already been assembled to evaluate the global temperature and every global expression is the assembly of elemental expression, the only term that needs to be evaluated for thermal sensitivity is $\frac{\mathcal{D}\mathbf{R}}{\mathcal{D}\phi_i}$. Differentiation of Equation (1.5) yields:

$$\begin{aligned}
\frac{\mathcal{D}\mathbf{R}}{\mathcal{D}\phi_i} &= \sum_V \left\{ \left[\frac{\partial \mathbf{B}^T}{\partial \phi_i}\mathbf{kB}\,{}^n\mathbf{T} + \mathbf{B}^T\mathbf{k}\frac{\partial \mathbf{B}}{\partial \phi_i}\,{}^n\mathbf{T} + \mathbf{B}^T\frac{\partial \mathbf{k}}{\partial \phi_i}\mathbf{B}\,{}^n\mathbf{T} - \mathbf{N}^T\frac{\partial Q}{\partial \phi_i} \right. \right. \\
&\quad \left. +\mathbf{N}^T\mathbf{N}\frac{\partial \rho C_p}{\partial \phi_i}\frac{{}^n\mathbf{T} - {}^{n-1}\mathbf{T}}{{}^n t - {}^{n-1}t} + \mathbf{N}^T\mathbf{N}\rho C_p\frac{-1}{{}^n t - {}^{n-1}t} \right] WJ \\
&\quad + \left[\mathbf{B}^T\mathbf{kB}\,{}^n\mathbf{T} - \mathbf{N}^T Q + \mathbf{N}^T\mathbf{N}\rho C_p\frac{{}^n\mathbf{T} - {}^{n-1}\mathbf{T}}{{}^n t - {}^{n-1}t} \right] W\frac{\partial J}{\partial \phi_i} \right\} \\
&\quad + \sum_{A_q} \left[\mathbf{N}^T\frac{\partial q}{\partial \phi_i}wj + \mathbf{N}^T qw\frac{\partial j}{\partial \phi_i} \right]
\end{aligned} \tag{1.27}$$

1.3.2 Mechanical Sensitivity

In this section, it is assumed that temperatures and their sensitivities are available (Equation (1.27)). Further, mechanical forces are not considered, that is, temperature change is the only loading in this sensitivity formulation. The left superscript n is dropped for simplicity.

Primary Sensitivity

Differentiating the global residual equation with respect to each design variable ϕ_i yields

$$\frac{d\mathcal{U}}{d\phi_i} = -\left\{ \left[\frac{d\mathcal{R}}{d\mathcal{U}}\right]^{-1}_{constant\ \phi_i} \right\} \frac{\mathcal{DR}}{\mathcal{D}\phi_i} \tag{1.28}$$

where $\mathcal{D}$ stands for the variance due to all variables but $\mathcal{U}$. Similar to the thermal sensitivity formulation, the only term that needs to be evaluated for displacement sensitivity is $\frac{\mathcal{DR}}{\mathcal{D}\phi_i}$, which is:

$$\frac{\mathcal{DR}}{\mathcal{D}\phi_i} = \sum_V \left[\frac{d\mathbf{B}^T}{d\phi_i}\sigma wJ + \mathbf{B}^T\frac{\mathcal{D}\sigma}{\mathcal{D}\phi_i}wJ + \mathbf{B}^T\sigma w\frac{dJ}{d\phi_i} \right] \tag{1.29}$$

In case of non-active yielding:

$$\frac{\mathcal{D}\sigma}{\mathcal{D}\phi_i} = \frac{\mathcal{D}\sigma_B}{\mathcal{D}\phi_i} \tag{1.30}$$

In case of active yielding, σ can be expressed as follows from the radial return algorithm

$$\sigma = \sigma_h + \sigma_Y \mathbf{m} \tag{1.31}$$

where σ_h is the hydrostatic stress of σ. Then $\frac{\mathcal{D}\sigma}{\mathcal{D}\phi_i}$ is evaluated as follows

$$\frac{\mathcal{D}\sigma}{\mathcal{D}\phi_i} = \frac{\mathcal{D}\sigma_h}{\mathcal{D}\phi_i} + \sigma_Y\frac{\mathcal{D}\mathbf{m}}{\mathcal{D}\phi_i} + \mathbf{m}\frac{\mathcal{D}\sigma_Y}{\mathcal{D}\phi_i} \tag{1.32}$$

Secondary Sensitivities

The secondary sensitivities can be evaluated only after the displacement sensitivity $\frac{d\mathbf{U}}{d\phi_i}$ is evaluated. In case of non-active yielding, σ_B and ϵ_{Be} are equal to σ and ϵ_e.

$$\frac{d\sigma}{d\phi_i} = \frac{d\sigma_B}{d\phi_i} = \frac{\partial\sigma_B}{\partial\mathbf{U}}\frac{d\mathbf{U}}{d\phi_i} + \frac{\mathcal{D}\sigma_B}{\mathcal{D}\phi_i} \tag{1.33}$$

$$\frac{d\epsilon_e}{d\phi_i} = \frac{d\epsilon_{Be}}{d\phi_i} = \frac{\partial\epsilon_{Be}}{\partial\mathbf{U}}\frac{d\mathbf{U}}{d\phi_i} + \frac{\mathcal{D}\epsilon_{Be}}{\mathcal{D}\phi_i} \tag{1.34}$$

$$\frac{d\epsilon_q}{d\phi_i} = \frac{d^{n-1}\epsilon_q}{d\phi_i} \tag{1.35}$$

In case of active yielding, the secondary sensitivities are evaluated as follows

$$\frac{d\sigma}{d\phi_i} = \frac{\partial\sigma}{\partial\mathbf{U}}\frac{d\mathbf{U}}{d\phi_i} + \frac{\mathcal{D}\sigma}{\mathcal{D}\phi_i} \tag{1.36}$$

$$\frac{d\epsilon_e}{d\phi_i} = \frac{\partial\epsilon_e}{\partial\mathbf{U}}\frac{d\mathbf{U}}{d\phi_i} + \frac{\mathcal{D}\epsilon_e}{\mathcal{D}\phi_i} \tag{1.37}$$

$$\frac{d\epsilon_q}{d\phi_i} = \frac{\partial\epsilon_q}{\partial\mathbf{U}}\frac{d\mathbf{U}}{d\phi_i} + \frac{\mathcal{D}\epsilon_q}{\mathcal{D}\phi_i} \tag{1.38}$$

Following relation can be obtained from Equation (1.20), Equation (1.22) and Equation (1.24):

$$\epsilon_e = \epsilon_{Be} - \Delta\epsilon_p = \epsilon_{Be} - \Delta\epsilon_q\frac{3}{2}\mathbf{Lm} \tag{1.39}$$

Using Equation (1.31) and Equation (1.39), the unknowns in Equation (1.36), Equation (1.37) and Equation (1.38) can be evaluated.

1.4 Numerical Implementation

Welding causes the material to have a permanent distortion and residual stress [11, 12, 8, 13]. The transient thermal tensioning also known as side heating technique can be used to control the welding distortion and residual stress without modifying design specification [14, 15]. There are many design variables that characterize the side heaters such as the heat source, position and shape of side heaters. In this section, the heat source and positions of side heaters are optimized with other variables fixed for the minimum residual stress using the sensitivity equations developed in the previous section in a 3D Lagrangian reference frame. No constraints are considered in this example.
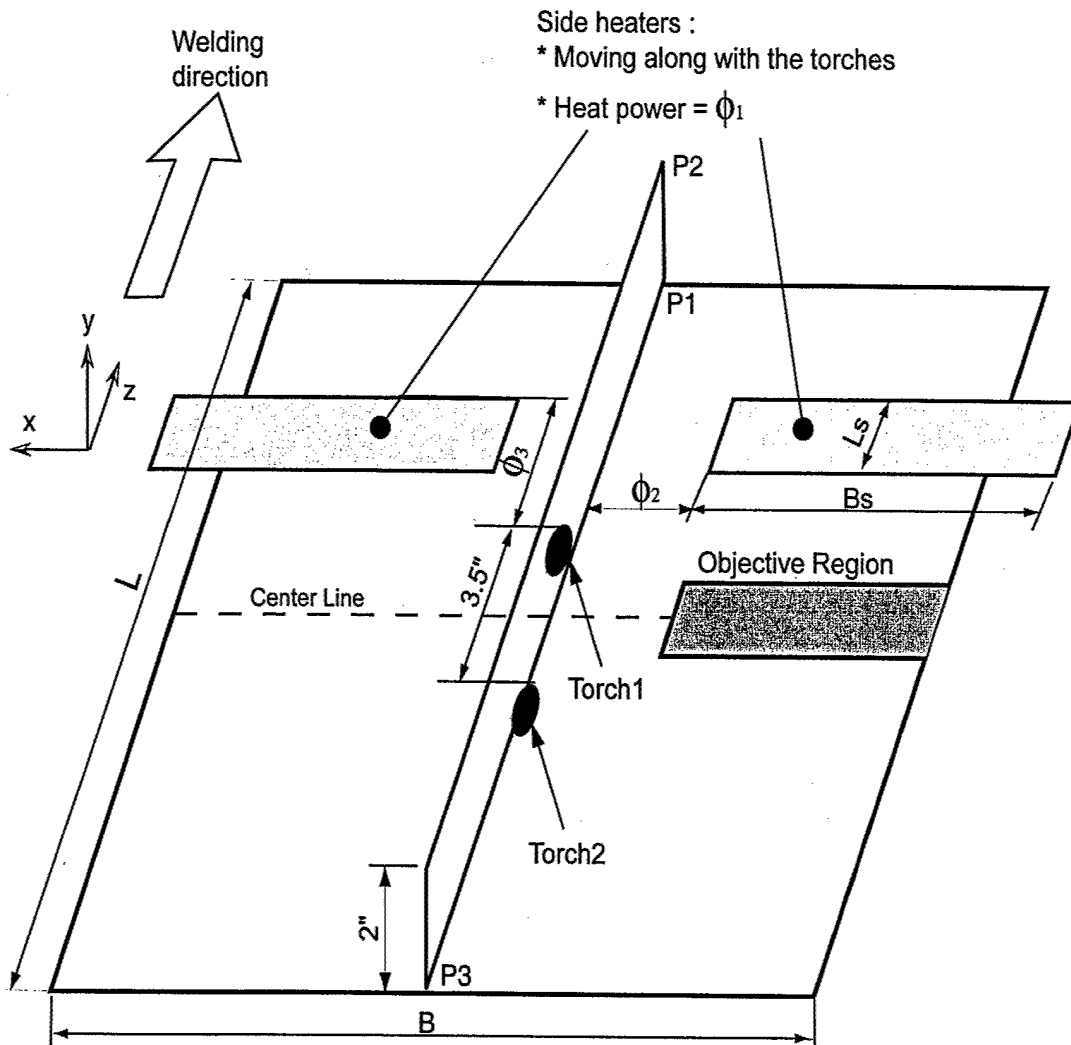
1.4.1 Welding Conditions

Figure 1.1: Configuration of welding and side heating setup.

The schematic welding configuration in this simulation is shown in the Fig 1.1. Side heaters

are followed by two welding torches.   Convection boundary conditions are assigned for all free
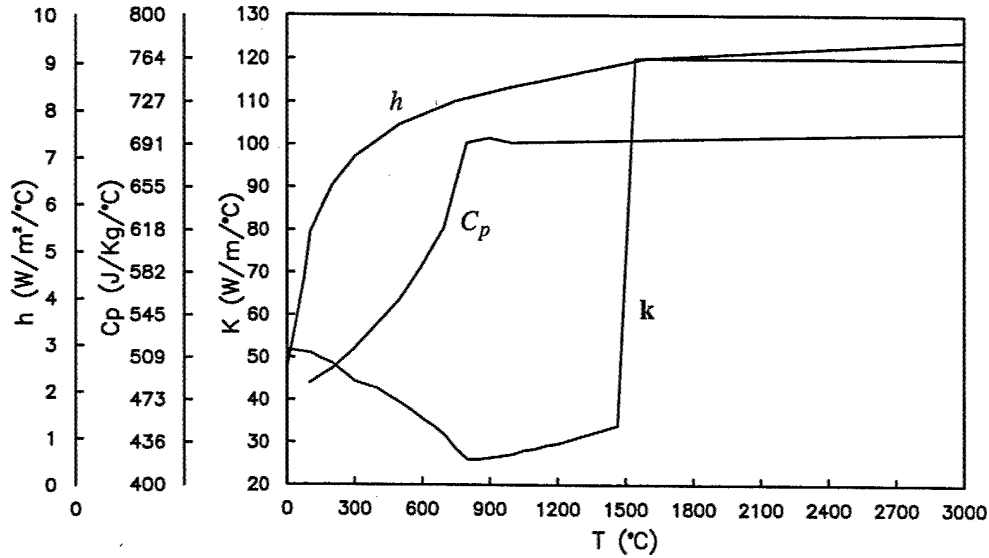

Figure 1.2: Conductivity (**k**), specific heat (C_p), and air convection (h) for A36.

surfaces. The internal heat generation rate by the welding torch, modeled with a "double ellipsoid" heat source model [16], is given as,

$$Q = \frac{6\sqrt{3}Q_w \eta_w f}{abc\pi\sqrt{\pi}} \, e^{-[\frac{3x^2}{a^2} + \frac{3y^2}{b^2} + \frac{3z^2}{c^2}]} \qquad [W/mm^3] \qquad (1.40)$$

where Q_w (2680.35 W/mm^3) is the welding heat input; η_w (1.0) is the welding efficiency, x, y, and z are the local coordinates of the double ellipsoid model aligned with the weld fillet; a ($5\sqrt{2}$ mm) is the weld width; b ($5\sqrt{2}$ mm) is the weld penetration; c is the weld ellipsoid length; v (6.35 mm/s) is the torch travel speed. The numbers in the parentheses are the values which are used for this implementation. Goldak et al. [16] used $c = a$ and $f = 0.6$ before the torch passes the analysis region, and $c = 4a$ and $f = 1.4$ after the torch pases the analysis region. However in this paper, $c = 4a$ and $f = 1.0$ are used instead to improve the convergence in the simulation. In fact, these factors have a measurable effect on the temperature field. However they have negligible effect on the residual stress. The side heat source is applied on the top surface of the plate as shown in Fig 1.1 and is defined as follows

$$\bar{q}(x,z) \;\; = \;\; \frac{Q_s \eta_s}{2B_s L_s} M_x M_z \qquad (1.41)$$

$$M_x \;\; = \;\; \{\tanh\left(S_{x2}[x + \phi_2 + B_s/2]\right) - \tanh\left(S_{x1}[x + \phi_2 - B_s/2]\right)$$
$$+ \tanh\left(S_{x1}[x - \phi_2 + B_s/2]\right) - \tanh\left(S_{x2}[x - \phi_2 - B_s/2]\right)\} /2 \qquad (1.42)$$

$$M_z \;\; = \;\; \{\tanh\left(S_{z1}[z - L_s/2]\right) - \tanh\left(S_{z2}[z + L_s/2]\right)\} /2 \qquad (1.43)$$

where x and z are the local coordinates from the center of the side heating; $Q_s(W/mm^2)$ is the side heating input, η_s (1.0) is the side heating efficiency; B_s (6") and L_s(1") are the band width and length of the side heating, S_{x1} (0.2), S_{x2} (0.2), S_{z1} (0.2) and S_{z2} (0.2) are used to control the gradient of heat flux in the side heater edges. This side heater shape is shown in Figure 1.4.
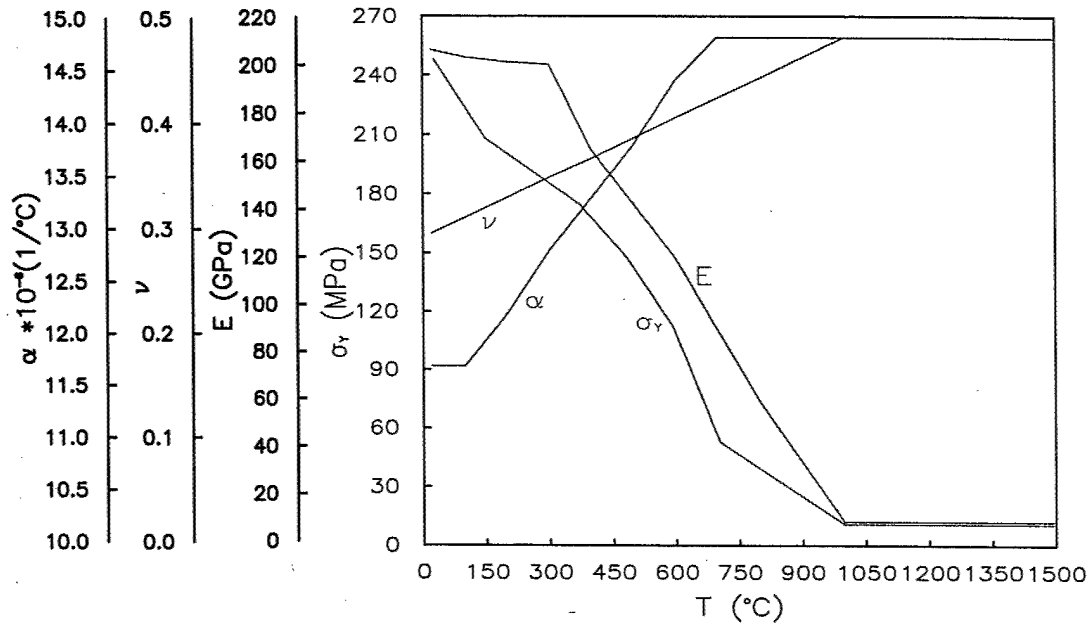
Figure 1.3: Elastic modulus (E), Poission's ratio (ν), thermal expansion coefficient (α) and yield strength (σ_Y) for A36.

The numbers in the parentheses are the values which are used in this simulation. The material properties of A36 steel used in this simulation are shown in Figure 1.2 for the thermal analysis and in Figure 1.3 for the mechanical analysis. The isotropic hardening coefficient is assumed to be 8000 [MPa] at any temperature.
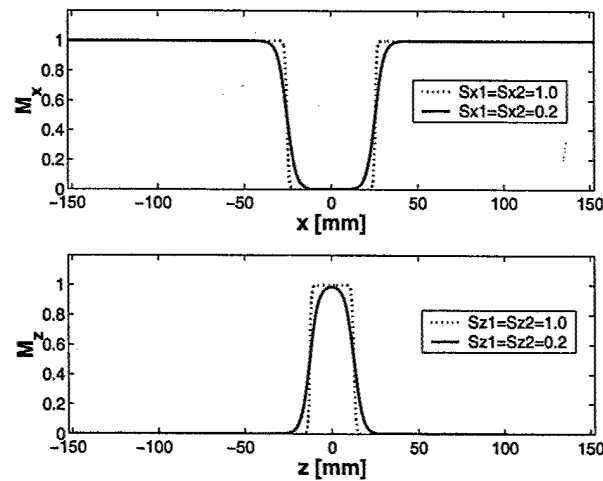

Figure 1.4: Side heater shape parameters M_x and M_z (see Equation (1.42) and Equation (1.43))

A finite element model is developed as shown Figure 1.5. The dimensions are 12" × 12" × 1/8" for base plate and 12" × 2" × 1/8" for the stiffener. This model has 13864 nodes and 2352 20-noded brick elements. Since high temperature gradients are prevalent at the welding region, the mesh is finer along the welding torch path and coarser away from it. The boundary conditions for the mechanical analysis are shown in Table 1.1.
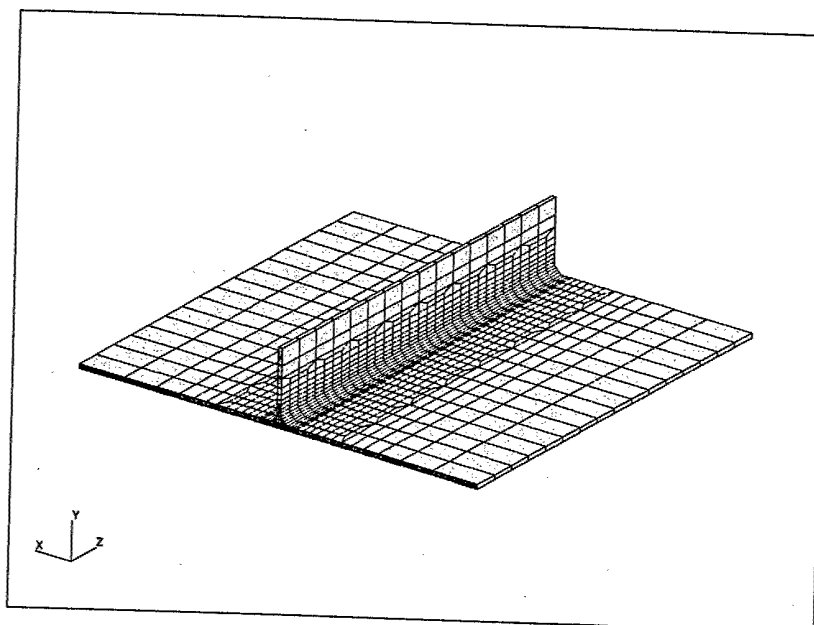
Figure 1.5: 3D Lagrangian analysis model : 12" × 12" × 1/8"

Constrained point	Displacement constrained direction
P1	X Y Z
P2	X
P3	X Y

Table 1.1: Boundary conditions for the mechanical analysis (see Figure 1.1 for P1, P2 and P3).

1.4.2 Optimization

Since the residual longitudinal compressive stress away from the weld zone can be used as a criterion of welding induced buckling [17], the optimization problem is expressed as follows

$$\min F = \min \sum_e (l^e \sigma_{zz}^e)^2 \tag{1.44}$$

$$(\phi_i)_{min} \leq \phi_i \leq (\phi_i)_{max} \tag{1.45}$$

where σ_{zz}^e is the centroid longitudinal residual stress at element e in the objective region shown in Figure 1.1, and l^e is the x-direction length of the element. The gradient of the objective function F is obtained as follows.

$$\frac{\partial F}{\partial \phi_i} = 2 \sum_e (l^e)^2 \sigma_{zz}^e \frac{\partial \sigma_{zz}^e}{\partial \phi_i} \tag{1.46}$$

The Design variables are the side heat source $Q_s(= \phi_1)$, transverse position of the side heater ϕ_2 and the distance between the side heater and the first welding torch ϕ_3 as shown in Equation (1.41) and Figure 1.1.

The optimization loop is implemented using the BFGS line search method provided in the DOT package [18].

Thermal and mechanical analyses and their sensitivity analyses are performed in an in-house SMP FORTRAN 90 code.

1.4.3 Results

The results of the numerical optimization are summarized in Table 1.2. The total analysis time for each side heating configuration is set up to 3000 seconds for both the thermal and mechanical analyses because temperature distribution becomes uniform and the residual stress distribution shows no more change after that time. Since a transient analysis has many incremental results, the figures shown in this paper are selected at only one increment. The result plots of temperature analysis are chosen when all the heat sources appear in the analysis model and those of mechanical analysis at the final increment.

The temperature profile at the initial design point is shown Figure 1.6. The sensitivity of the temperature field with respect to the side heat source at the initial design point is shown in Figure 1.7. Increase in side heat source will result in temperature increase in the side panel. The longitudinal residual stress profile at the initial design point is shown in Figure 1.8. The stress is tensile near the welding torch path and compressive away from it. Figure 1.9 shows the longitudinal residual sensitivities with respect to the side heat source. The stress in the objective region (see Figure 1.1) is compressive as shown in Figure 1.8 so that positive sensitivity is the desirable direction for the minimum residual stress in that region.

The longitudinal residual stress field with the optimum design variables is shown in Figure 1.10. Compared with Figure 1.8, the residual stress reduction is observed not only in the objective region but also over the outside panel. Figure 1.11 shows the longitudinal residual stresses along the "Center Line" (see Figure 1.1) for three cases. The residual stress in the objective region is successfully reduced for the optimum side heater. The vertical dotted-line in the left side from the axis line indicates where the objective region start.

The variation of the objective function defined in Equation (1.44) during this optimization is shown in Figure 1.12. A total of 28 function calls and 6 gradient calls were made during entire optimization.

Design Variable	Initial Val.	Minimum	Maximum	Optimum
ϕ_1 : Heat input (Q_s) $[W]$	5000.00	0.00	10000.00	9288.01
ϕ_2 : Side offset $[mm]$	50.80	0.00	150.00	54.24
ϕ_3 : Long. offset $[mm]$	50.80	-100.00	100.00	47.00

Table 1.2: Design variables (see Figure 1.1)

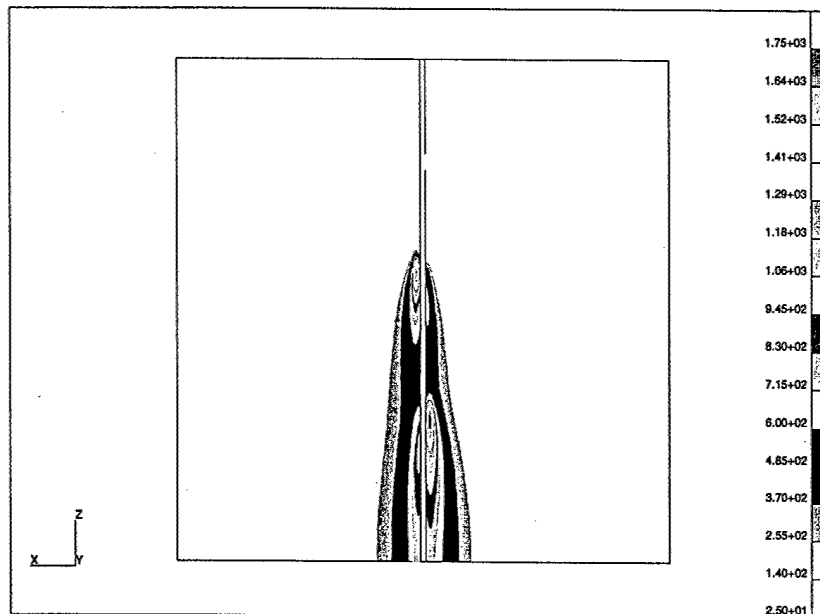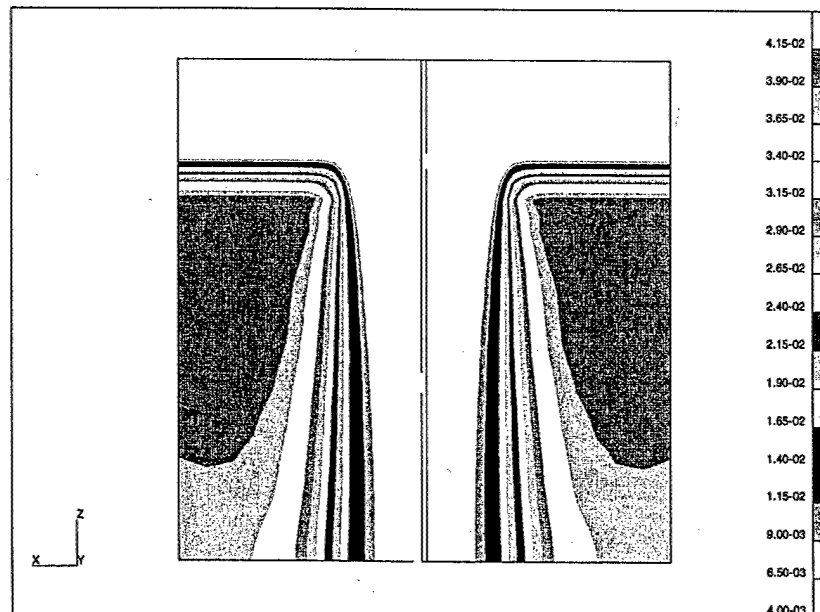Figure 1.6: Temperature profile at the initial design point [°C]

Figure 1.7: Sensitivity of temperature with respect to side heat source (ϕ_1) at the initial design point [°C/W]
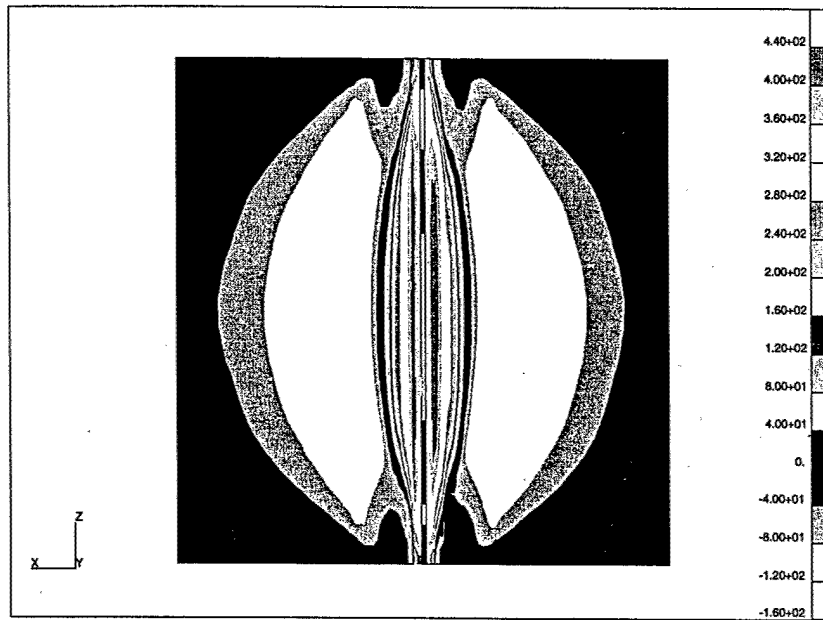
Figure 1.8: Longitudinal residual stress at the initial design point [MPa]

Figure 1.9: Sensitivity of longitudinal residual stress with respect to side heat source (ϕ_1) at the initial design point [MPa/W]

Figure 1.10: Longitudinal residual stress at the optimum design point [MPa]
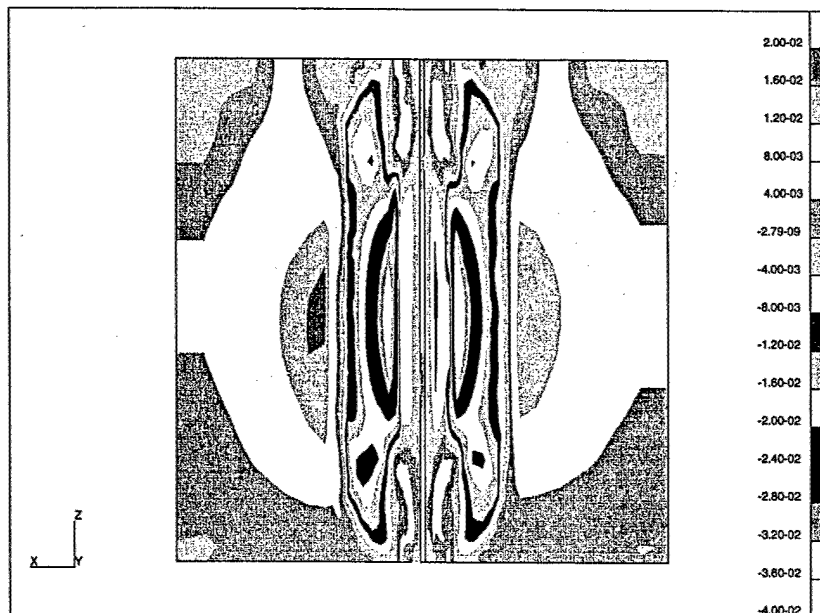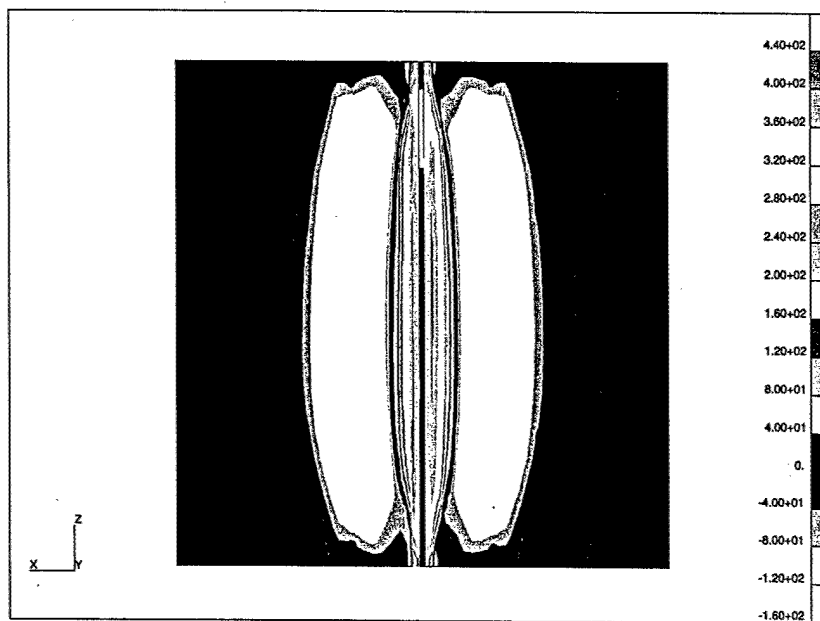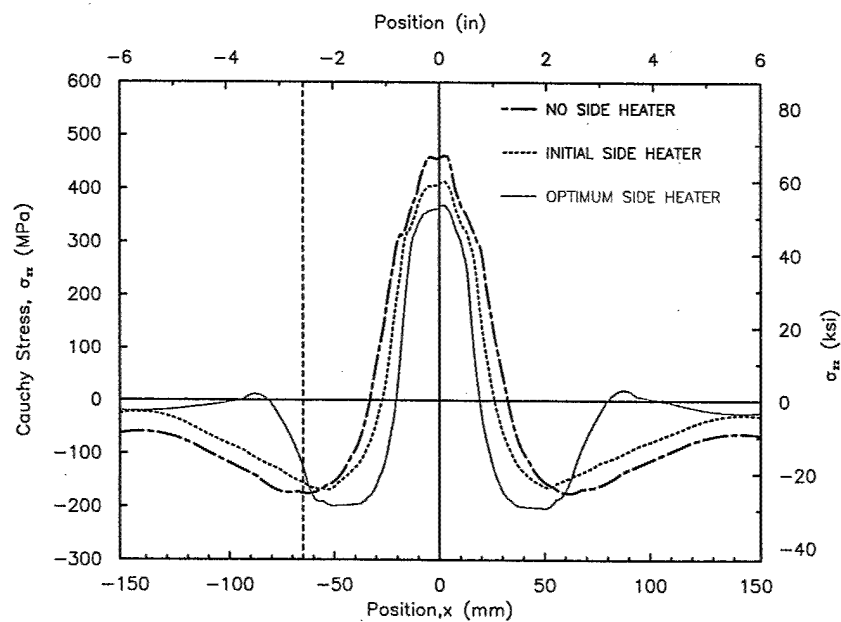

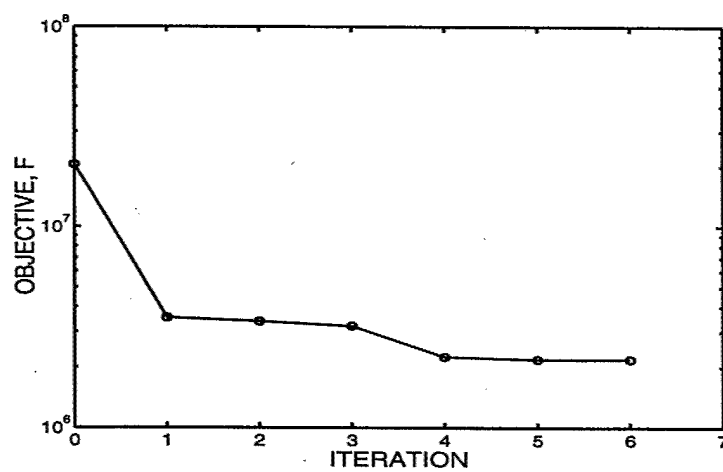Figure 1.11: Longitudinal residual stress comparison along the "Center Line" (see Figure 1.1)

Figure 1.12: Variation of the objective function F during optimization (see Equation (1.44)) $[(mm \cdot MPa)^2]$

Chapter 2

Prediction of Buckling and Bowing Welding Distortion in Large Structures

2.1 Introduction

Due to the advantages in design flexibility, cost savings, reduced overall weight and enhanced structural performance, welding has been applied increasingly in comparison with other mechanical joining processes. However, several types of distortion can be induced, as discussed in detail by Masubuchi [19] (Figure 2.1), with the application of welding process.
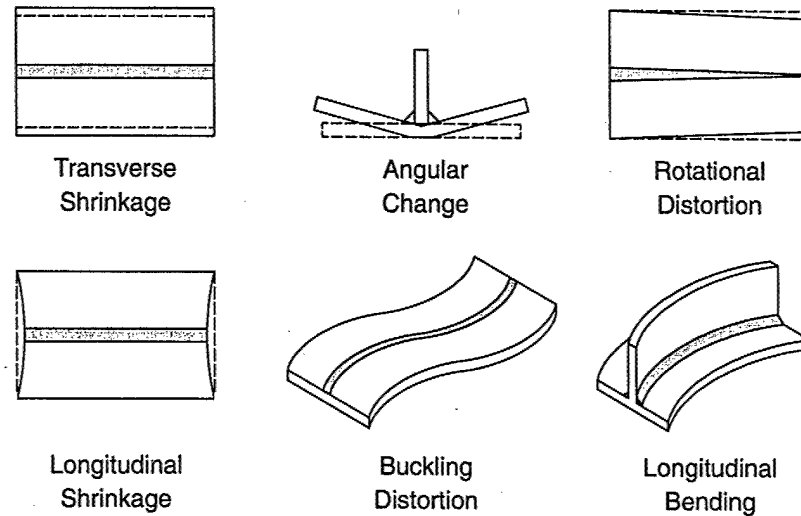

Figure 2.1: Types of welding distortion [19].

Among the types of distortions, the out-of-plane deformations, such as bending, buckling and angular deformations, significantly influence the required dimensional precision in structural components. In order to acquire reduction in overall weight and achieve more controllable manufacturing, relatively thin components made of higher strength steels are preferred when fabricating large structures. However, welding in thinner components introduces a significant drawback, namely out-of-plane distortions. These types of distortions cause loss of dimensional control, structural integrity, fit-up between panels, and thus increase fabrication costs. Consequently, analysis on the out-of-plane distortion effects is important in many industries such as shipbuilding, railroad, aerospace, and mass rapid transportation systems.

Finite element techniques have been used in the prediction of welding residual stress and distortion for more than two decades. Due to the nature of the process, additional complexities are involved in the FEA of welding compared to traditional mechanics, such as temperature and history dependent material properties; high gradients of temperature, stress and strain fields with respect to both time and spatial coordinates; large deformations in thin structures and phase transformation and creep phenomena. Welding-induced buckling of thin-walled structures has been investigated in greater detail in [20, 21, 22]. Ueda et. al. [20, 23] presented a methodology to determine the buckling behavior of plates by large deformation elastic FEA and employing inherent strain distributions. Michaleris et. al. [21, 24] developed a predictive buckling analysis technique for thin section panels, combining decoupled weld process simulations and eigenvalue buckling analyses. Tsai et. al. [22] studied the distortion mechanisms and the effect of welding sequence on panel distortion. No published work is available for the computation of the combined effects of both

bending and buckling distortion.

Michaleris *et al.* [25], demonstrated that 3D finite element models of the welding process are needed to accurately compute angular distortion. Furthermore, 3D weld process finite element models can easily account for the increased stiffness of plate curvature and the compliance of fixturing restrains. However, 3D finite element simulations of welding large structures require very large models where heat balance and equilibrium is iteratively computed for several thousand increments [26]. Such simulations would require prohibitively costly numerical computations using currently available software. The development of an efficient computational approach is needed for performing direct 3D welding simulations.

In this work the decoupled 2-D and 3-D finite element analysis technique by Michaleris et. al. [24, 21] is applied to evaluate welding-induced longitudinal bending and buckling in various stages of the fabrication of the maglev guideway beam. Longitudinal residual stress effects are considered only, and the angular distortion which usually has small magnitude [17] is neglected. It is demonstrated that 1) eigenvalue analyses can only compute the critical buckling stress that induces the buckling distortion as well as the various buckling modes, 2) small deformation analyses only compute the bending effect on the structure and the deformation magnitude, and 3) large deformation analyses can compute the combined effects of bending and buckling and the deformation magnitude.

The Maglev system is a high-speed magnetically levitated ground transportation system that is designed to operate at speeds in excess of 310 mph at a high level of ride comfort. The system has no wheels or moving parts and is levitated and propelled by a long stator linear motor embedded in the guideway. Both propulsion and levitation are provided by electro-magnetic waves resulting in a system that moves contact free, with no wear and tear on the system and no friction to impede its efficiency. In order to achieve high ride comfort at speeds in excess of 310 mph, guideway structure must be manufactured within very small tolerances. The 47-mile proposed Pennsylvania alignment consists of over 2000 guideway beams, each measuring 203 feet long, weighing 135 tons with compound curves built-in and having to be manufactured within millimeters of tolerance. Precision fabrication technology needs to be developed for the production of the guideway beam within specifications.

Figure 2.2 shows a section of the maglev guideway beam, which is the main component of the magnetic levitation transportation system. The guideway beam is double span and is supported by piers with varying distances between them depending on the beam type and curvature. The section of a beam known as the Type 1 guideway beam is analyzed in this work. As shown in Figure 2.2, the guideway beam is a trapezoidal box beam structure with 25 mm thick stiffeners located at fixed intervals. The main components are the top flange, also known as the 'deck plate', which is 18 mm thick, the side web plates which are 12 mm thick and the bottom flange which is 30 mm thick. The top flange, side web plates and bottom flange are welded longitudinally using fillet welds. The stiffeners are welded onto the top flange using double fillet welds.

Dimensional accuracy is especially important in maglev guideway beam technology to achieve high level of ride comfort. Therefore, the out-of-plane distortions resulting from welding, such as bending, buckling and angular deformations, need to be kept at a minimum. Furthermore, if buckling distortion occurs, the structural instability resulting from the out-of-plane distortion violates the tolerance requirements. This results in either reduced quality in passenger transportation, or even re-manufacturing of the structure which detrimentally increases manufacturing cost.
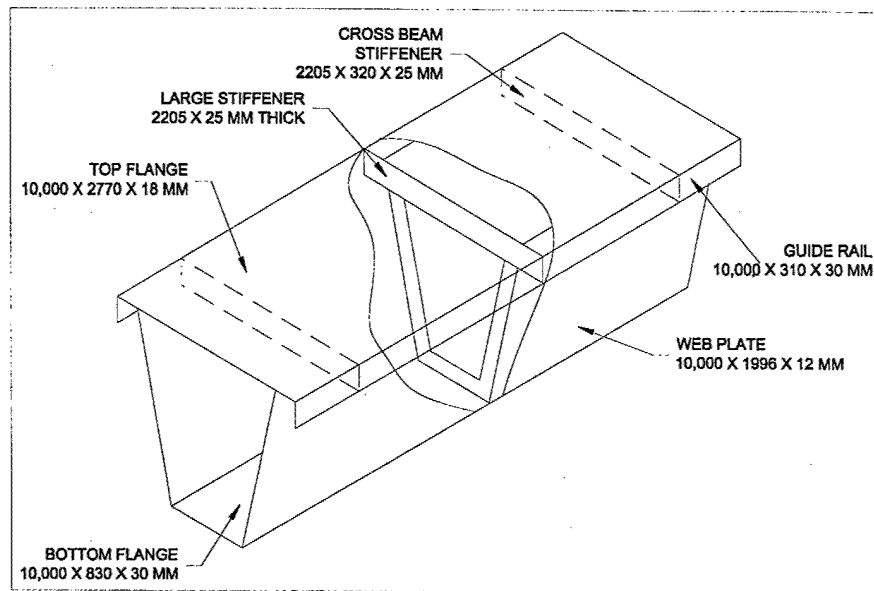
Figure 2.2: The components of the maglev guideway beam

2.2 Analysis Approaches

Following the work of Michaleris et. al. [24, 21], the response of the maglev guideway beam is evaluated in two steps by combining three-dimensional structural analyses with two-dimensional welding simulations in a decoupled approach. The longitudinal residual stresses only are considered, while the angular distortion is neglected.

2-D Thermo-mechanical Weld Simulation :

A two dimensional thermo-elasto-plastic analysis is performed to determine the residual stress, and plastic strain fields during the welding process. The longitudinal residual stresses are caused by the negative plastic strains resulting from the welding thermal cycle.

3-D Structural Deformation Simulation and Eigenvalue Analysis :

The longitudinal bending (bowing) and buckling distortion effects are consequently determined by applying the, mostly uniform and compressive, longitudinal plastic strain field of the 2-D weld model on the 3-D structural model as equivalent load.

A constant, negative thermal load is applied at the weld region to introduce the effects of welding into the 3-D structure. Thermal loading is used rather than mapping the plastic strain field, which would require a complex mapping procedure.

The deformation analyses are performed with applications of linear (small deformation) and non-linear (large deformation) formulations, respectively. With the linear structural deformation analysis only, the bowing distortion magnitude induced by applying the welding can be evaluated. Meanwhile, the combined bowing and buckling distortion magnitude can be shown in the non-linear results.

An eigenvalue analysis is performed to determine the critical residual stresses. The various buckling distortion modes can also be attained.

2.2.1 Welding Simulation

The welding simulation involves a thermal and a mechanical analysis. The effect of mechanical response is assumed to be negligible on the thermal behavior, thus the temperature field is solved independently from the mechanical solution. To determine the temperature history profile, a non-linear, transient heat-flow finite element analysis is performed on the plane perpendicular to the welding direction.

Thermal Analysis

The numerical implementation of the history dependent (transient) heat transfer problem involves an incremental scheme with several small time increments. This analysis procedure is addressed in detail in references [27, 28, 29].

The governing energy balance equation for transient heat transfer analysis is given as follows,

$$\rho C_p \frac{dT}{dt}(\mathbf{r}, t) = -\nabla_{\mathbf{r}} \cdot \mathbf{q}(\mathbf{r}, t) + Q(\mathbf{r}, t) \qquad \text{in the entire volume } V_{\mathbf{r}} \text{ of the material} \qquad (2.1)$$

where ρ is the density of the body ([$7,820 kg/m^3$]), C_p is the specific heat capacity, T is the temperature ([^oC]), $\mathbf{q}$ is the heat flux vector, Q is the internal heat generation rate, t is the time, $\mathbf{r}$ is the coordinate in the reference configuration and $\nabla_{\mathbf{r}}$ is the spatial gradient operator. Material properties for medium carbon steel (A36) are used in this study [30].

Convection boundary conditions are assigned for all free surfaces. The internal heat generation rate by the welding torch, modeled with a "double ellipsoid" heat source model [16], is given as,

$$Q = \frac{6\sqrt{3}Q_b(\eta)f}{abc\pi\sqrt{\pi}} e^{-[\frac{3x^2}{a^2} + \frac{3y^2}{b^2} + \frac{3(z+vt)^2}{c^2}]} \qquad [W/mm^3] \qquad (2.2)$$

where Q_b is the welding heat input; η is the welding efficiency, x, y, and z are the local coordinates of the double ellipsoid model aligned with the weld fillet; a is the weld width; b is the weld penetration; $c = 4a$ is the weld ellipsoid length, and $f = 0.6$ when the torch is behind the analysis plane, and $f = 1.4$ after the torch passes the analysis plane; v is the torch travel speed; and t is time.

Elasto-plastic Mechanical Analysis

The subsequent history dependent stress analysis is performed by modelling the stress problem as a quasi-static process in a Lagrangian frame. This problem has been covered by several investigators [3, 7, 4, 2, 31].

The temperature values solved in the previous thermal analysis are imported to the mechanical analysis as loading. Generalized plane-strain conditions are assumed to account for the out-of-plane expansion in the structure. The longitudinal (out-of-plane) strain ϵ_z is assumed to vary linearly with x- and y- coordinates in the analysis plane:

$$\epsilon_z = e - x\phi_y + y\phi_x \qquad (2.3)$$

where e is the z-component of the strain at the coordinate origin and the constants ϕ_x and ϕ_y represent the strain variations in the y and x axes, respectively.

The stress equilibrium equation is given by,

$$\nabla_{\mathbf{r}}\boldsymbol{\sigma}(\mathbf{r},t) + \mathbf{b}(\mathbf{r},t) = 0 \qquad \text{in } V_{\mathbf{r}} \tag{2.4}$$

where σ is the stress, $\mathbf{b}$ the body force, and t is time. The mechanical constitutive law is :

$$\dot{\boldsymbol{\sigma}} = \mathbf{C}\,(\dot{\epsilon} - \dot{\epsilon}_p - \dot{\epsilon}_t) \tag{2.5}$$

$$\dot{\epsilon}_p = \dot{\epsilon}_q \cdot \mathbf{a}\,(\sigma, \epsilon_{\mathbf{q}}, T) \tag{2.6}$$

$$f = \sigma_e - \sigma_y \leq 0 \tag{2.7}$$

where T is temperature, $\mathbf{C}$ is the material stiffness tensor, $\mathbf{a}$ is the plastic flow vector, ϵ, ϵ_p and ϵ_t are the total, plastic and thermal strains and ϵ_q is the equivalent plastic strain. In Equation (2.7), f is the yield function, σ_e is the Von Misses stress, and σ_y is the yield stress. Active yielding occurs when $f = 0$. The mechanical material properties are assumed for A36 [30].

Weld Scaling Factor

The longitudinal residual stress is positive at the weld region and negative elsewhere. This stress distribution is caused by a negative longitudinal plastic strain at the weld region. Instead of applying the exact plastic strain distribution on the 3-D structure, a negative unit thermal load is applied at the welding region.

A 2-D linear analysis with a unit thermal load is performed to determine the scaling factor to the unit load that produces equivalent longitudinal stress to the welding residual stress. With the acquired longitudinal residual stresses at the free edges, σ_{res} in the weld simulation and σ_1 in the unit thermal load analysis respectively, the scaling factor is evaluated as

$$\gamma = \sigma_{res}/\sigma_1 \tag{2.8}$$

2.2.2 Structural Analysis

3-D Small Deformation Analysis:
The small deformation (linear) analysis is defined as follows [32, 33]:

$$\mathbf{Ku} = \mathbf{f} \tag{2.9}$$

where $\mathbf{K}$ represents the linear stiffness matrix, $\mathbf{f}$ represents the nodal load vector, and $\mathbf{u}$ is the nodal displacement vector.

The linear deformation analysis is performed with applying a negative thermal load ($\mathbf{T} = -\gamma$). Due to the assumption of the linear relationship between load and displacement, the analysis is accomplished by applying the (thermal) load in one step to acquire the deformation magnitude.

3-D Large Deformation Analysis:
The large (non-linear) deformation analysis is defined as solving the following equation for $\mathbf{u}$ [32, 33]

$$(\mathbf{K} + \mathbf{K_G})\mathbf{u} = \mathbf{f} \tag{2.10}$$

where $\mathbf{K}$ and $\mathbf{K_G}$ represent the linear and non-linear (stress stiffening) stiffness matrices, respectively. $\mathbf{f}$ represents the nodal load vector, and $\mathbf{u}$ is the nodal displacement vector.

A negative thermal load ($\mathbf{T} = -\gamma$) is applied. Unlike the linear analysis which can be accomplished in one step, the large deformation analysis is performed incrementally with the applied load divided into small increments.

3-D Eigenvalue Buckling Analysis:

The elastic instability problem is defined as an eigenvalue problem as follows [32, 33]

$$det \, (\, \mathbf{K} + \lambda \mathbf{K_G} \,) = 0 \tag{2.11}$$

where $\mathbf{K}$ and $\mathbf{K_G}$ are the linear and non-linear (stress stiffening) stress stiffness matrices, and λ is the eigenvalue.

A 3-D eigenvalue analysis is performed on the structural model with a unit negative thermal load applied in the weld region ($T = -1.0$) to model the uniform compressive longitudinal plastic strain field occurring in welding. The eigenvalues (λ_i) represent the multipliers (scaling factors) which result in the critical buckling stress field ($\sigma_{cr})_i$ when multiplied with the stress field resulting from the unit thermal load (σ_L).

$$(\sigma_{cr})_i = \lambda_i \cdot \sigma_L \qquad \text{[MPa]} \tag{2.12}$$

The buckling distortion is determined from the eigenvectors (mode shapes) of the structure. The structure may buckle in any of the modes with critical stresses lower than the residual stress field due to welding. It will tend to buckle with the permissible buckling mode having the lowest critical stress. The permissibility of the modes is determined by the constraints on the structure. If certain buckling modes are suppressed by the mechanical fixturing applied, the structure will tend to buckle the next available (higher) mode.

2.3 Maglev guideway beam modelling

Dimensions of the Model

The actual length of the guideway beam utilized in this project is 61.92 m. As the beam has a uniform cross section and consists of alternating diaphragm and crossbeam stiffeners at equally spaced intervals of approximately 3 m, only a portion of the beam is analyzed to simplify the analysis. The portion analyzed has a length of 9.804m and contains one end-bearing diaphragm, 2 crossbeam stiffeners and one large diaphragm. The boundary conditions used are as follows: 1) The x- translation displacement is set to be 0 on node a (Figure 2.5) 2) The x- and y- translation displacements are set to be 0 at node b (Figure 2.5) 3) The z-translation displacement and the x- and y- rotational displacements are set to 0 on all nodes at the cut plane (symmetry B.C.)

The entire length of maglev guideway beam, utilized in this analyzed project is 200 feet (61 meters) long. In order to simplify the analysis model, a portion of length 9.804 m which contains one end-bearing diaphragm, one diaphragm and two cross-beam stiffeners inside the portion is considered. In the analyzed models, the boundary conditions are as follows : 1) x-translational displacement is set to be 0 at node a,(Figure 2.5) 2) x- and y- translational displacements are set to be 0 at node b,(Figure 2.5) 3) z-translational displacement and x- and y- rotational displacements are set 0 at all nodes on the cut (symmetry b.c.) plane.

Welding Sequence

As the current manufacturing approach is to tack weld the stiffeners and the web plates onto the top flange plate before welding, the same is assumed in the analysis. Since the structure is elastic, the model is analyzed with the static stresses applied simultaneously to the structure.

Analysis Cases

To examine the effect of the guide rails on the maglev guideway beam if the structure is manufactured sequentially, analyses are performed for two models: one with and the other without guide rails. The analysis models are shown in Figures 2.5 and 2.6, respectively.

2.3.1 2-D model and welding simulation Simulation

The 2-D thermo-mechanical analysis is performed to determine the scaling factor from welding to be applied. The boundary conditions utilized in this analysis are shown in Figure 2.3. The inclined plate represents the 12 mm web plate and the bottom plate represents the 30mm bottom flange. The heat from welding at the fillet is applied as a heat source as per Equation (2.2). All the free surfaces are the convective surfaces. The node on the bottom left corner is restrained in all degrees of freedom and the node on the web plate top canter is restrained in the x direction to prevent rotation. The 2-D finite element mesh in the heat transfer and mechanical analysis of the panel is illustrated in Figure 2.4. The model consists of 339 8-noded quadrilateral quadratic elements with 1136 nodes. The finite element solutions are performed using an SMP in-house Fortran90 finite element code.
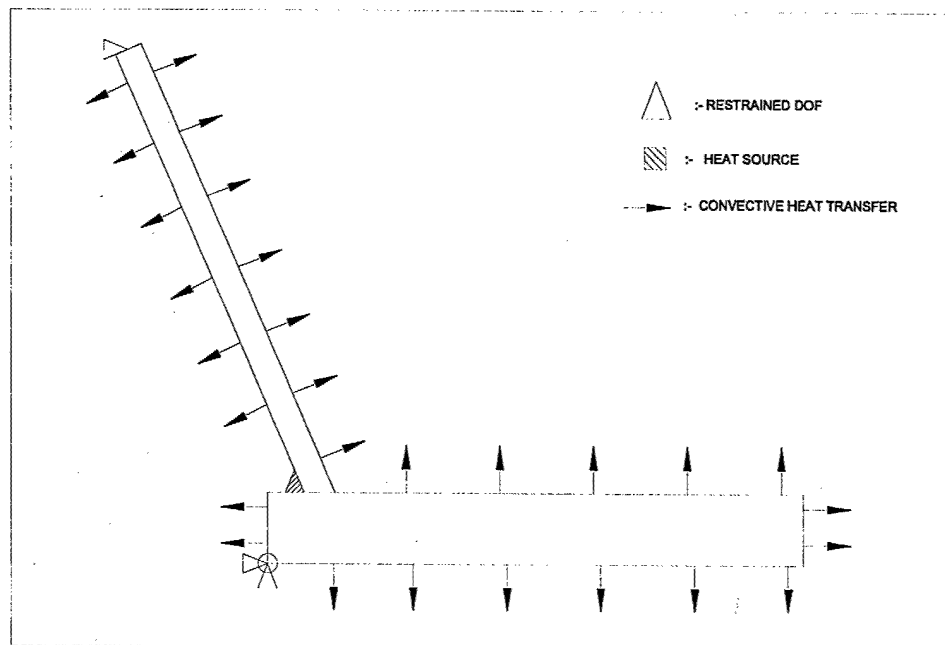
Weld Simulation

Figure 2.3: Boundary Conditions for 2-D welding simulation models

Thermo-mechanical analysis of unit thermal load

2-D generalized plane strain models are developed to compute the stress σ_L resulting from a unit thermal load. The same 2D mesh as in earlier case is used for this analysis. A negative unit load is applied in the weld zone. Ambient temperature is applied at all other nodes.

2.3.2 3-D Structural Analysis

Two cases were analyzed: The first model had the guide rails and consisted of a total of 1691 nodes and 1948 elements, including 1658 (4-noded) shell elements and 290 truss elements (Figure 2.5). The second model did not have the guide rails and consisted of a total of 1539 nodes and 1726 elements, including 1510 shell elements and 216 truss elements (Figure 2.6). The truss elements represent the weld zone and the thermal loads are applied to the truss elements. Both the deformation and buckling are performed on both models using the ABAQUS finite element software.
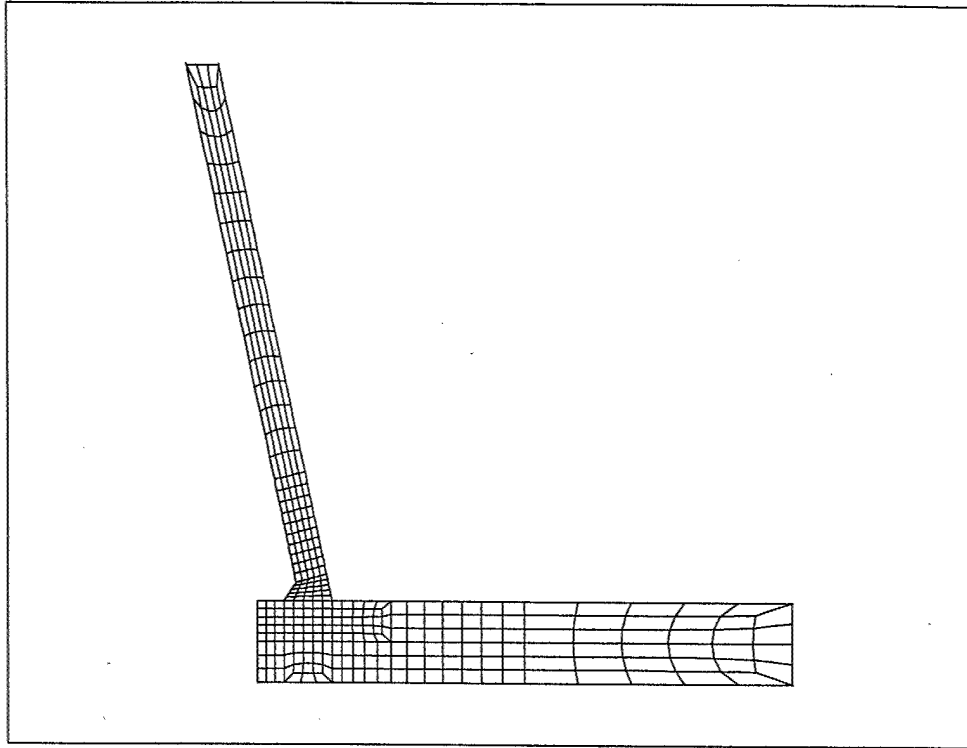
Figure 2.4: FEA mesh for 2-D welding process analysis

The thermal loads are applied at the truss elements. Based on the weld size, the cross-section area of the truss elements are $32mm^2$ along the line connecting guide rails and the top plate, $18mm^2$ along other welding lines except the elements at the cut (symmetry B.C.) plane which has $9mm^2$. The deformation and buckling analyses are performed by using ABAQUS software. No preload is applied in the analyses.

2.4 Results

2.4.1 2-D Analyses

Weld Simulation

Figure 2.7 shows the distribution of residual stresses in Z direction as computed by the 2-D simulation of welding. The stresses are tensile in the weld zone and in the heat affected zone. However, away from the weld zone, the stress changes the sign from tensile to compressive. The peak residual longitudinal stress at the weld center is 412 MPa and residual stress at the free edge is $\sigma_{res} = -12$ MPa. Figure 2.8 shows the plastic strain. All of the plastic strains are negative.

Unit Load

Figure 2.9 shows the distribution of stresses in Z direction for the 2D thermo-mechanical analysis due to the unit load. The maximum residual stress at the weld center is 0.94 MPa and that at the free edges is $\sigma_1 = -0.0322$ MPa. Thus, the multiplier γ (scaling factor) for welding applied on the model can be acquired as

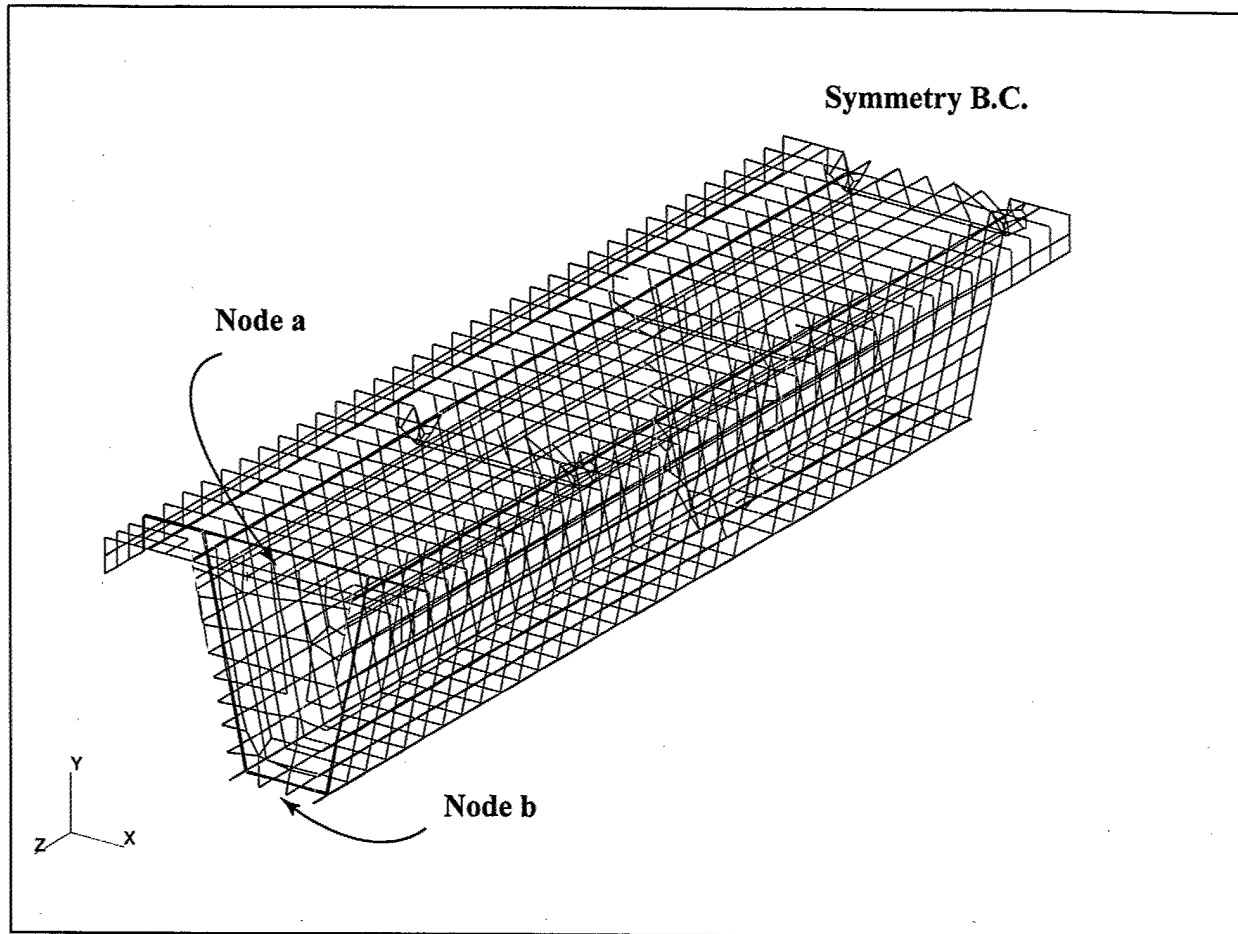$$\gamma = \frac{\sigma_{res}}{\sigma_1} = \frac{-12}{-0.0322} = 372 \tag{2.13}$$

Figure 2.5: FEA mesh for 3-D structural analysis in the case of with guide rails

2.4.2 3-D Analysis

Model with Guide Rails

Deformation Analysis

Figure 2.10 illustrates the small deformation and large deformation analysis results with 20X magnification. The linear analysis captures the bowing effect at the free end side. The large deformation analysis captures the combined effects of bowing and buckling.

Significant distortion is observed at the free end. Figure 2.11 shows the x-direction displacements along the guide rail edges, i.e. along line A and line B shown in Figure 2.10. The y-direction displacements along both longitudinal lines are shown in Figure 2.12.

Buckling Modes

The first four buckling modes of the model with guide rails are shown in Figure 2.13, where it is observed that the buckling deformation on the web flange are more evident than on the top flange.

The first and second eigenmodes can be categorized as one group with repeated eigenvalues, because those are basically the same type of buckling waves. The major difference, as shown in Figure 2.14, is that the first mode is symmetric about the YZ-plane while the second mode is anti-symmetric.
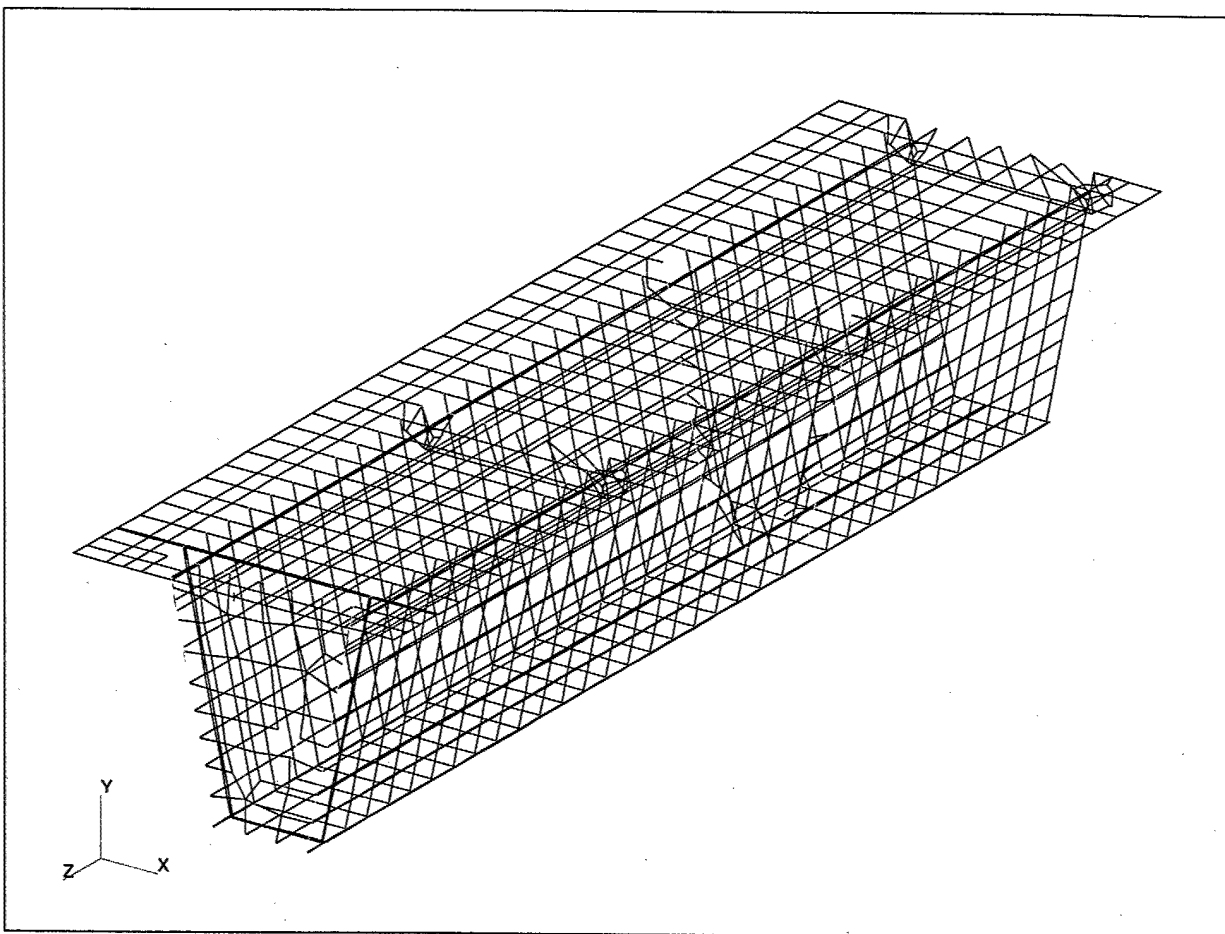
Figure 2.6: FEA mesh for 3-D structural analysis in the case of without guide rails

Model without Guide Rails

Deformation Analysis

The deformations in the model without guide rails are shown in Figure 2.15 for large deformation and linear analysis, respectively. Unlike the results in the case with guide rails, the deformation result of linear analysis shows that there is no bowing effect, because no welding load is applied on the lines designed to be connected with guide rails.

Buckling waves near the edges are observed on the top panel in the large deformation analysis result, because there are no constraints applied by the guide rails. Line C in Figure 2.15 represents the line where the guide rails are to be welded. Figure 2.16 shows the x- and y- direction displacements along the edge of the top plate, along the Line C in Figure 2.15.

Buckling Modes

The first four buckling modes of the model with guide rails are shown in Figure 2.17. Similar to the modes in the analysis case with guide rails, the buckling deformations are more evident on the side panels than on the top panel. However, compared with Figure 2.13, because guide rails are not present, the top panel has more deformation.

Similarl to the model with guide rails, repeated eigenvalues and corresponding eigenmodes are also observed.

Mode	w/ Guide Rails	w/o Guide Rails	Mode	w/ Guide Rails	w/o Guide Rails
1	98.989	114.92	16	159.34	181.92
	100.09	116.53		161.44	182.96
	108.00	124.01		165.70	189.55
	108.79	125.03		191.35	217.68
	110.99	127.04		194.15	221.67
6	111.99	128.05	21	222.18	255.87
	113.92	129.78		223.15	257.44
	116.75	132.74		234.63	269.67
	116.97	133.40		235.69	271.14
	119.77	138.63		266.78	278.04
11	124.45	143.79	26	269.87	297.88
	125.61	145.91		270.71	298.87
	150.75	168.38		274.10	307.73
	151.89	173.36		282.12	320.78
	156.32	174.18		295.09	327.11

Table 2.1: Comparison of eigenvalues in buckling eigenvalues below the scaling factor between different models

Mode	w/ Guide Rails	w/o Guide Rails
31	295.95	331.89
	298.86	337.94
	305.37	342.94
	306.03	351.36
	307.56	354.19
36	313.16	362.72
	317.88	368.26
	318.29	370.79
	320.21	371.83
	321.75	—
41	332.54	—
	334.63	—
	340.48	—
	347.23	—
	348.47	—
46	350.51	—
	351.56	—
	355.92	—
	360.37	—
	361.87	—
51	367.80	—

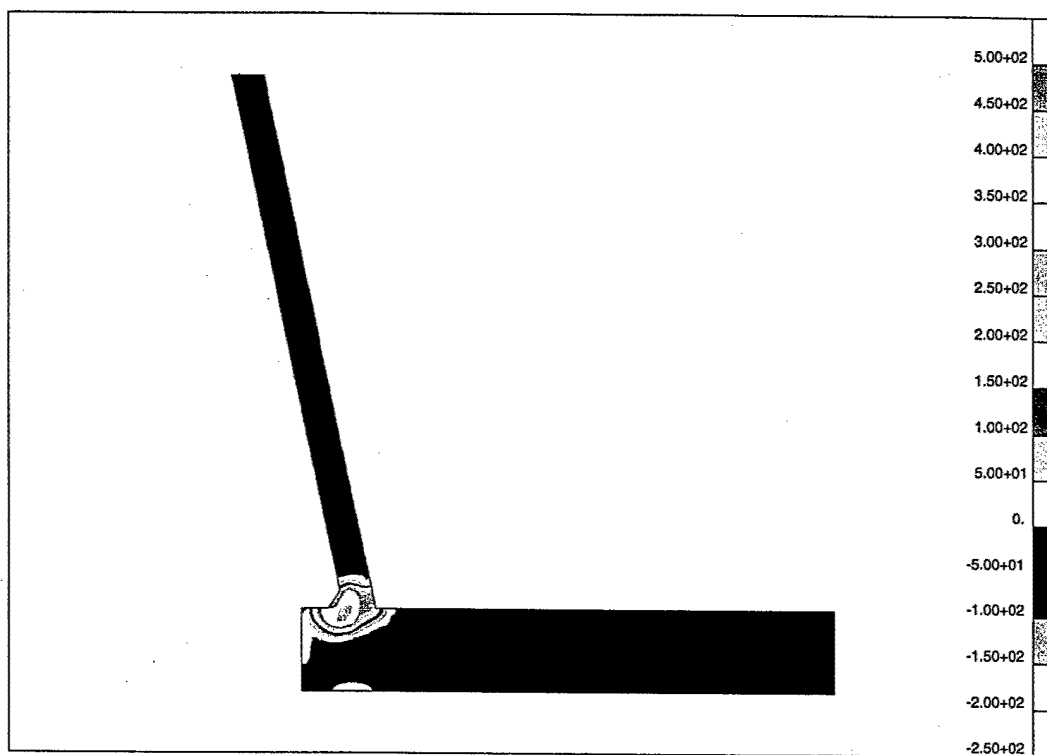Table 1: Comparison of eigenvalues in buckling eigenvalues below the scaling factor (Cont'd)

Figure 2.7: Longitudinal Residual Stress obtained from 2-D analysis (MPa)
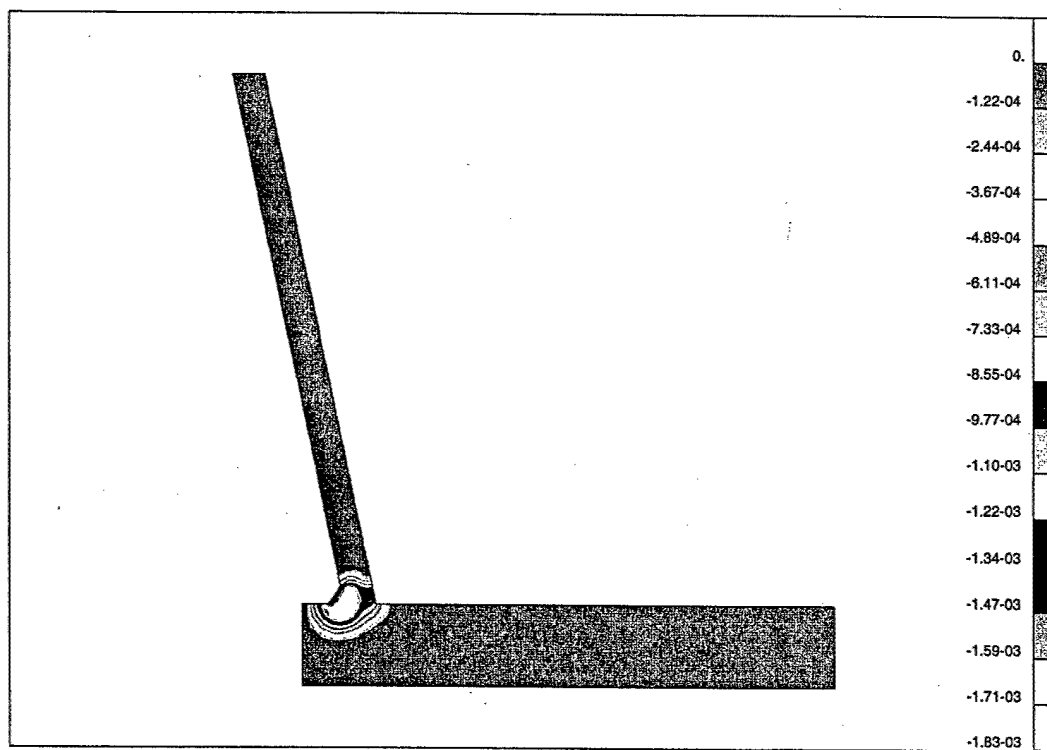

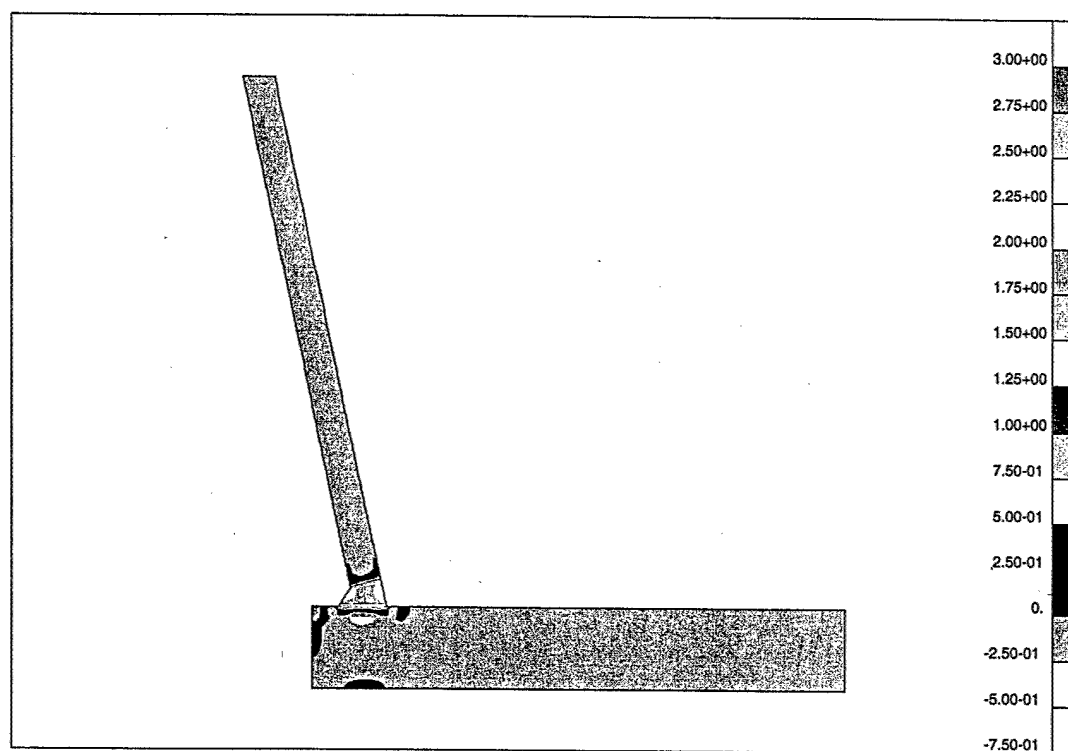Figure 2.8: Plastic Strain obtained from 2-D analysis

Figure 2.9: Longitudinal Residual Stress using Unit Load obtained from 2-D analysis (MPa)
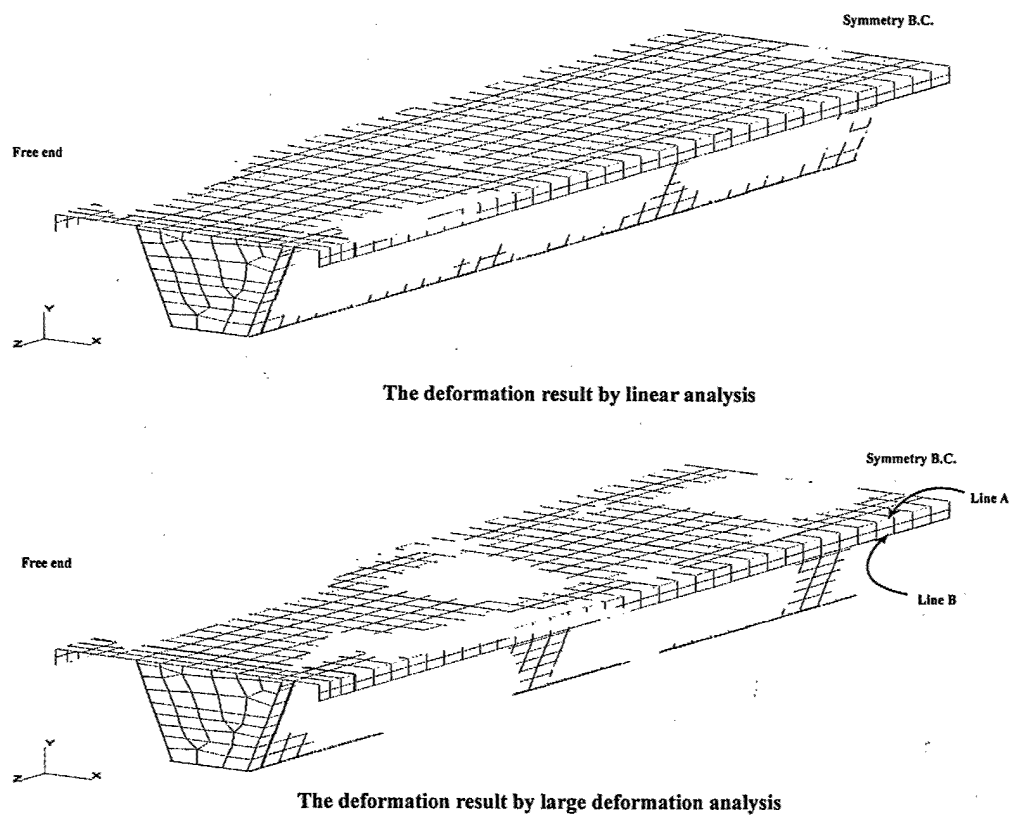
Figure 2.10: The Deformation Results of the Model with Guide Rails (20X)
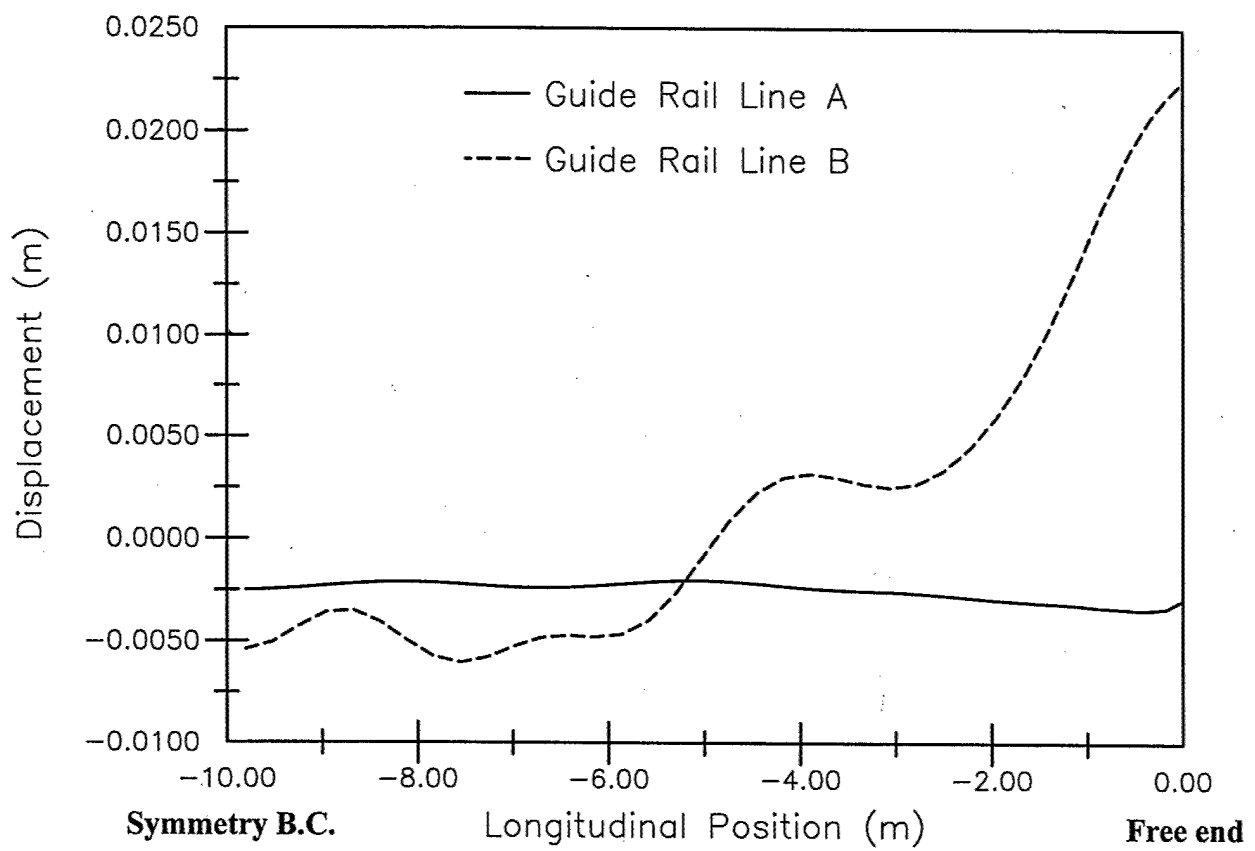
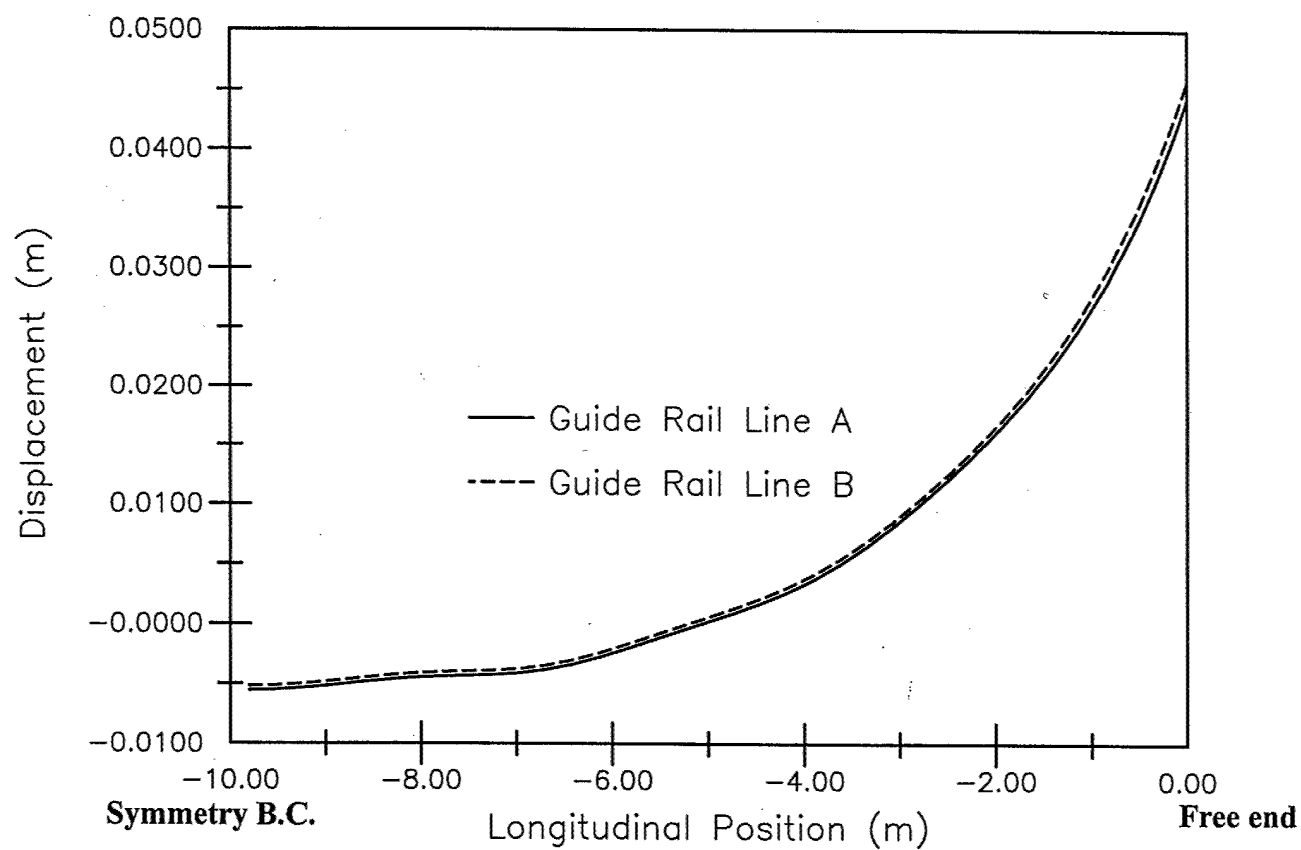Figure 2.11: X-direction Displacements of the Guide Rails

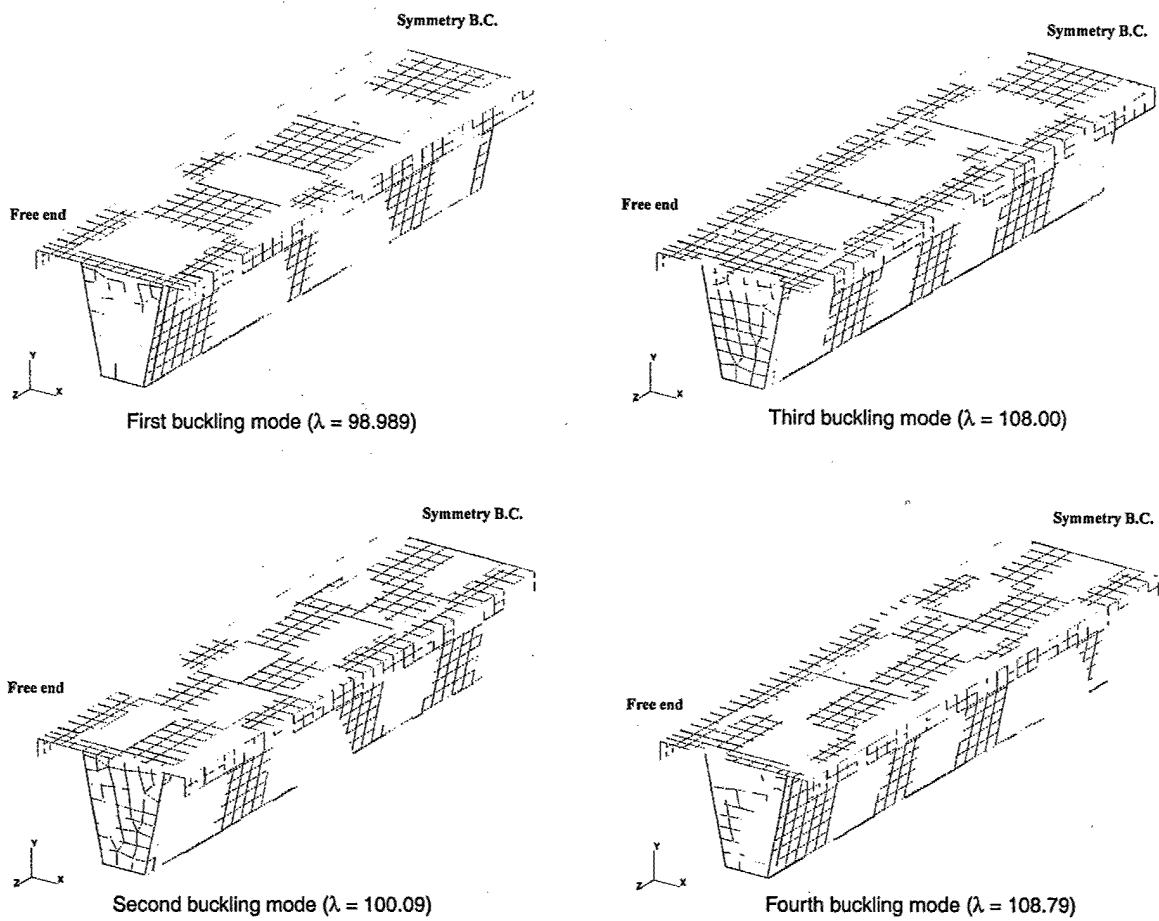Figure 2.12: Y-direction Displacements of the Guide Rails

Symmetry B.C.

Free end

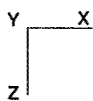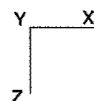First buckling mode (λ = 98.989)

Symmetry B.C.

Free end

Third buckling mode (λ = 108.00)

Symmetry B.C.

Free end

Second buckling mode (λ = 100.09)

Symmetry B.C.

Free end

Fourth buckling mode (λ = 108.79)

Figure 2.13: The First Four Buckling Modes for the Model with Guide Rails

Y ——— X

Z

The first buckling mode with top view

Y ——— X

Z

The second buckling mode with top view

Figure 2.14: First and Second Buckling Modes with Top View

Symmetry B.C.

Free end

The deformation result by linear analysis

Symmetry B.C.

Free end

Line C

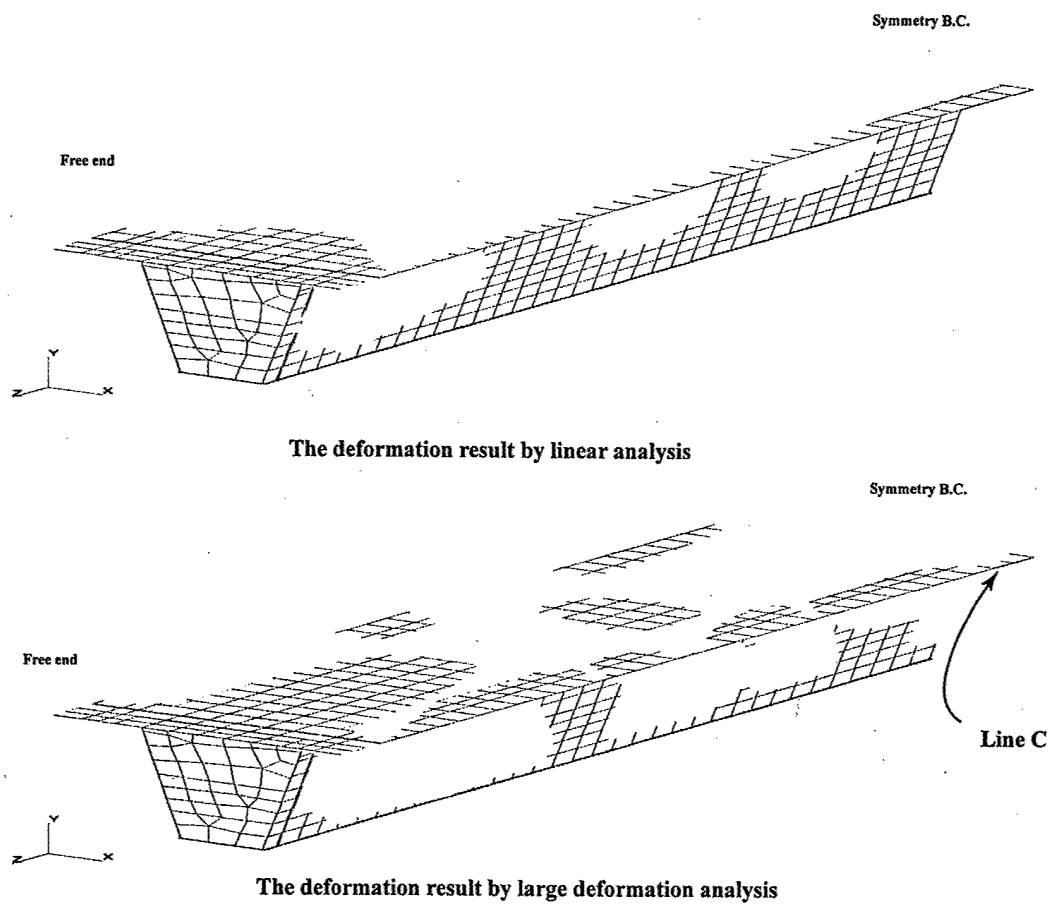**The deformation result by large deformation analysis**

Figure 2.15: The Deformation Results of the Model without Guide Rails (20X)
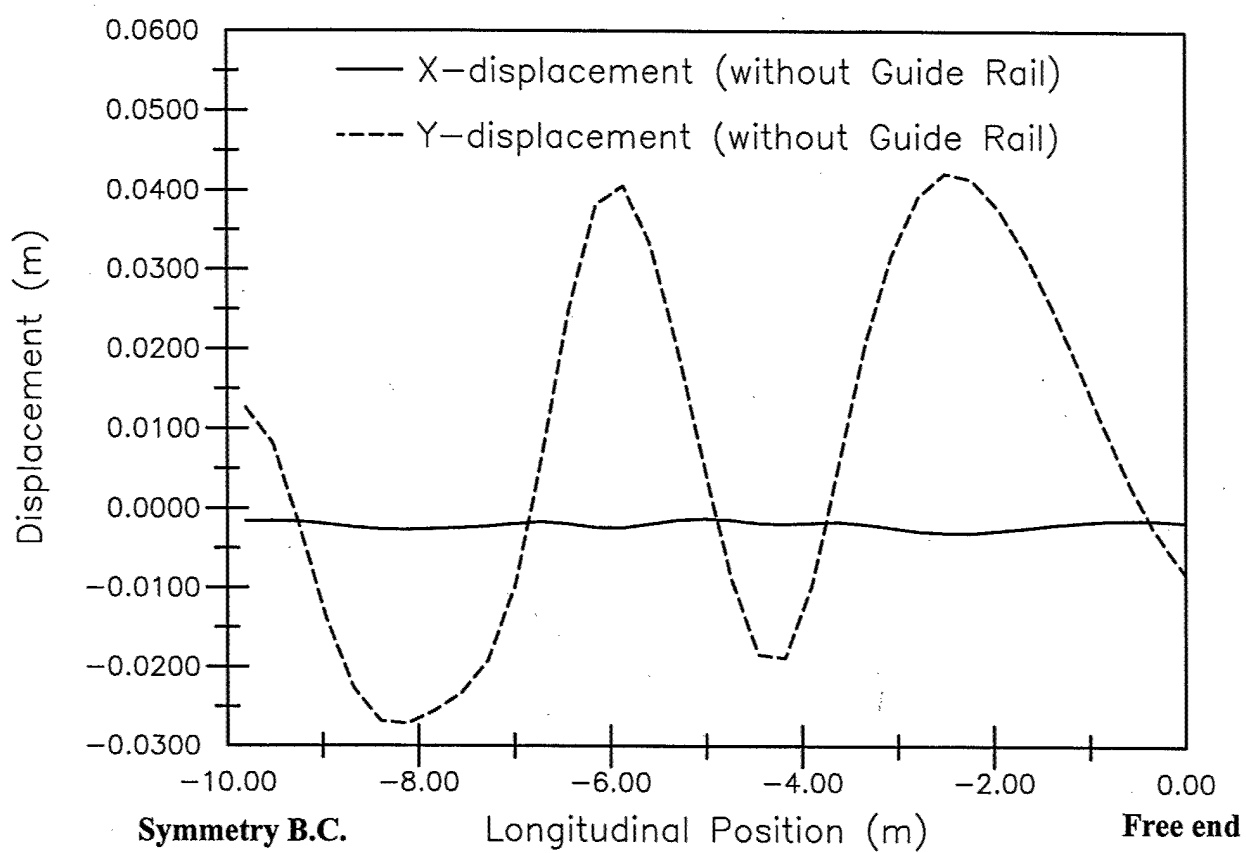
Figure 2.16: X- and Y- displacements on the line designed to connect the guide rails

First buckling mode (λ= 114.92)

Third buckling mode (λ = 124.01)

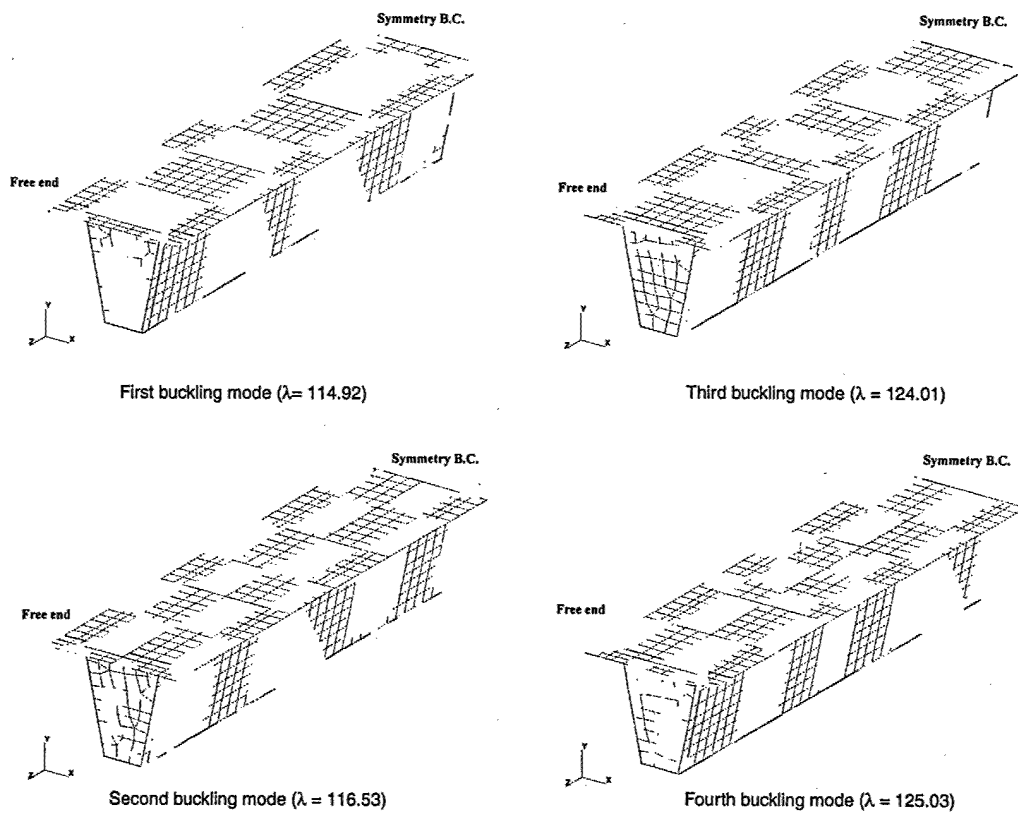Second buckling mode (λ = 116.53)

Fourth buckling mode (λ = 125.03)

Figure 2.17: The First Four Buckling Modes for the Model without Guide Rails

Chapter 3

Domain Decomposition and Adaptivity Methods

3.1 Domain Decomposition Method for Parallel Computing and Sensitivity Analysis

Motivation of Domain Decomposition Method:

- The practical engineering simulation problem is very large and complex
- The single computer power is limited and can not handle such a big job
- Parallel processing is introduced to resolve this issue
- Domain decomposition method is a native way to split problems for parallel processing

The nature of Dd method is divide and conquer. The domain is decomposed into several subdomains and they are assigned to individual processor. The shared boundary, or its related Lagrange multiplier equation is solved first, then the internal nodes in each subdomain. FETI methods is a family of iterative domain decomposition methods, it includes:

- FETI method [34]
- FETI-2 method [35, 36]
- FETI-Dual Primal method [37, 38]

The FETI Family Methods are numerically scalable for second and fourth order elasticity problems, such as plane stress, plane strain, solid mechanics, plate and shell problems. Each subdomain contains the nodes from the shared boundary, so connectivity between neighboring domains are enforced by introducing Lagrange multiplier, which forms the basic unknowns of interface equation. In FETI-Dual Primal methods, the displacement and rotation degrees of freedom from some corner nodes is also introduced as unknowns. Finally, the above equations is solved by an iterative method, such as preconditioned conjugate projected gradient method (PCPG).

When doing sensitivity analysis, since only the right hand side term is changed, it is preferred to have the direct inverse of stiffness matrix. FETI methods is not suitable here since it is based on iterative method. A similar domain decomposition method is used to make the calculation of inverse matrix easier, now all the degrees of freedom from the shared boundary forms the basic unknowns, and the corresponding equation is called Schur equation. The inverse of global stiffness matrix can be replaced by the inverse of each subdomain stiffness matrix and the inverse of Schur matrix.

An example of two subdomains is illustrated in Figure 3.1
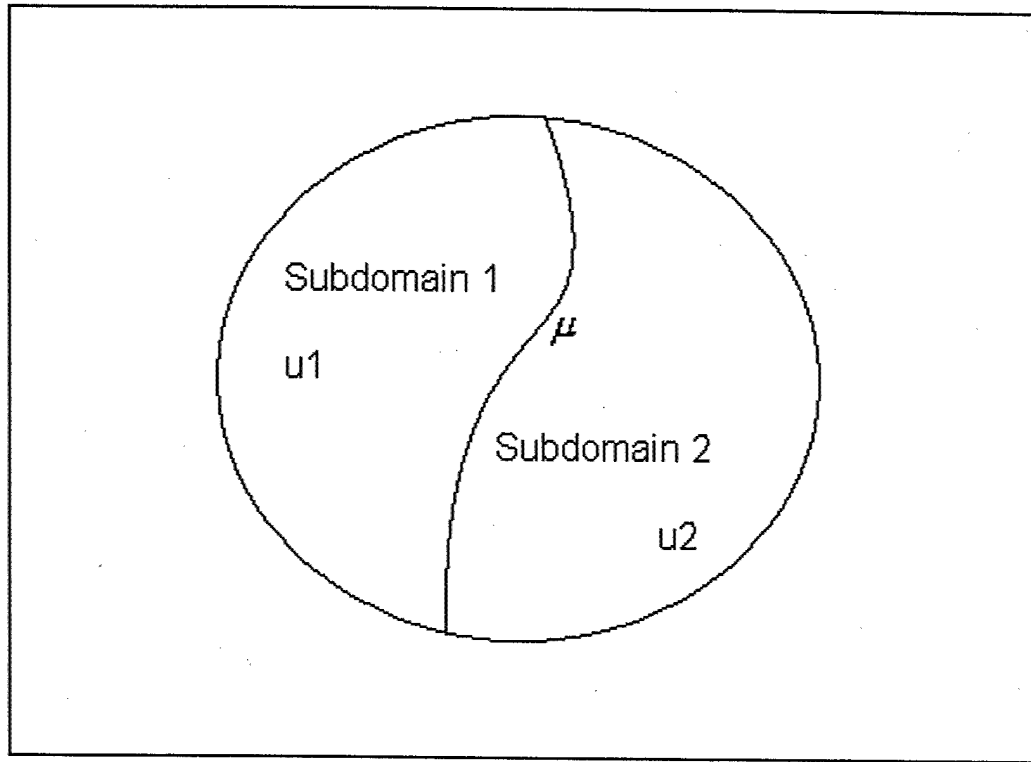
The finite element equation is as follows:

$$\begin{bmatrix} A_{11} & 0 & A_{13} \\ 0 & A_{22} & A_{23} \\ A_{13}^T & A_{23}^T & A_{33} \end{bmatrix} \begin{bmatrix} u_1 \\ u_2 \\ \mu \end{bmatrix} = \begin{bmatrix} f_1 \\ f_2 \\ f_B \end{bmatrix} \tag{3.1}$$

The Schur equation is derived by performing Gauss elimination on u_1, u_2

$$S\mu = \widetilde{f}_B \tag{3.2}$$

where,

$$S \equiv A_{33} - A_{13}^T A_{11}^{-1} A_{13} - A_{23}^T A_{22}^{-1} A_{23}$$

$$\widetilde{f}_B \equiv f_B - A_{13}^T A_{11}^{-1} f_1 - A_{23}^T A_{22}^{-1} f_2$$

Once μ is solved, we can derive u_1, u_2 from equation (3.1)

$$u_1 = A_{11}^{-1}(f_1 - A_{13}\mu) \qquad u_2 = A_{22}^{-1}(f_2 - A_{23}\mu)$$

To obtain the inverse matrix of this finite element equation, which is the same as solving this equation, we need to calculate three inverse matrices

$$A_{11}^{-1}, A_{22}^{-1}, \text{and } S^{-1}$$

this can be done by most direct solvers, like Watson solver and ESSL solver

Future Work on this topic will include the following:

- Testing on large and very large models
- Programming for sensitivity analysis
- Implement on distributed machines by using Message Passing Interface (MPI)

3.2 Adaptivity for Welding Simulations

Research has started for the implementation of adaptivity in welding simulations of large structures. A flow chard of the approach is illustrate in Figure 3.2. The approach is based on h-adaptivity using Lagrange multipliers to constrain incompatible elements.

$$\begin{pmatrix} \mathbf{K} & \mathbf{A} \\ \mathbf{A^T} & \mathbf{0} \end{pmatrix} \begin{pmatrix} \mathbf{u} \\ \lambda \end{pmatrix} = \begin{pmatrix} \mathbf{f'} \\ \mathbf{0} \end{pmatrix} \tag{3.3}$$

where, the original equation when there was no h-adaptivity applied is $\mathbf{K} * \mathbf{u} = \mathbf{f}$, λ is the Lagrange multipliers. The operator $\mathbf{A}$ is assembled with columns based on the mathematical relations of the dependent nodes among other nodes. For example, if $u_{node1} = \frac{1}{2}(u_{node2} + u_{node3})$,

$$\mathbf{A} = \begin{pmatrix} 1 & \cdots \\ -0.5 & \cdots \\ -0.5 & \cdots \\ \vdots & \ddots \end{pmatrix}$$
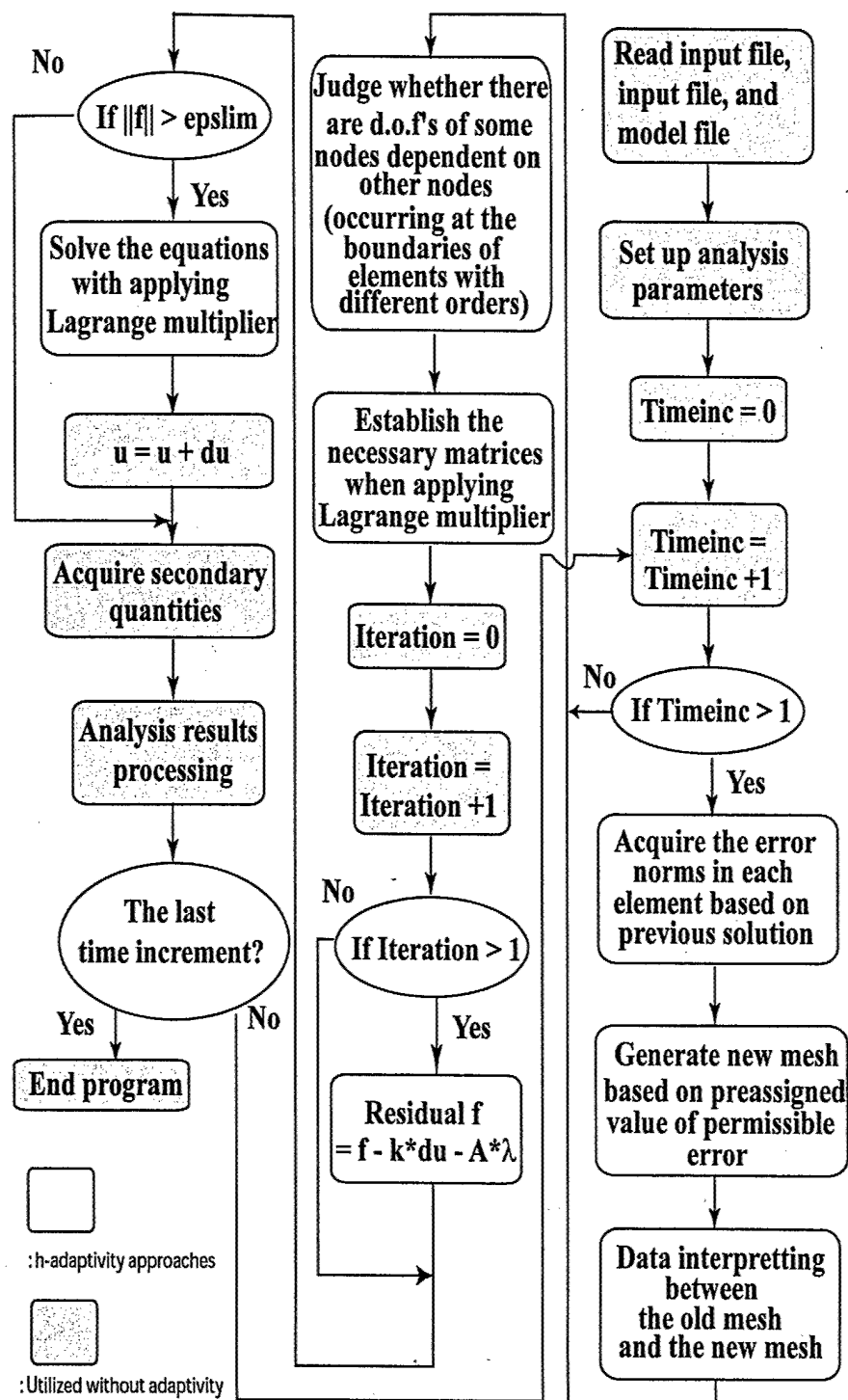
After rearrangement, Equation (3.3) will becomes

$$\begin{pmatrix} \mathbf{K} & \mathbf{A} \\ \mathbf{0} & -\mathbf{A^T K^{-1} A} \end{pmatrix} \begin{pmatrix} \mathbf{u} \\ \lambda \end{pmatrix} = \begin{pmatrix} \mathbf{f'} \\ -\mathbf{A^T K^{-1} f'} \end{pmatrix} \tag{3.4}$$

the left-hand side is in a form of an upper-triangle matrix. With the λ being evaluated, the $\mathbf{u}$ is then solved by

$$\mathbf{u} = \mathbf{K^{-1}(f' - A\lambda)} \tag{3.5}$$

Thus, the equation for applying h-adaptivity can be solved in an efficient way.

Further work is to test the whole procedure, combining the Lagrange multiplier procedure and refining elements, with heat transfer models and mechanical models.

No

If ||f|| > epslim

Yes

Solve the equations with applying Lagrange multiplier

$u = u + du$

Acquire secondary quantities

Analysis results processing

The last time increment?

Yes — End program

No

Judge whether there are d.o.f's of some nodes dependent on other nodes (occurring at the boundaries of elements with different orders)

Establish the necessary matrices when applying Lagrange multiplier

Iteration = 0

Iteration = Iteration +1

No

If Iteration > 1

Yes

Residual f = f - k*du - A*λ

Read input file, input file, and model file

Set up analysis parameters

Timeinc = 0

Timeinc = Timeinc +1

No

If Timeinc > 1

Yes

Acquire the error norms in each element based on previous solution

Generate new mesh based on preassigned value of permissible error

Data interpretting between the old mesh and the new mesh

□ : h-adaptivity approaches

▦ : Utilized without adaptivity

44

Bibliography

[1] J. C. Simo and R. L. Taylor. Consistent Tangent Operators for Rate-Independent Elasto-Plasticity. *Computer Methods in Applied Mechanics and Engineering*, 48:101–118, 1985.

[2] P. Tekriwal and J. Mazumder. Transient and Residual Thermal Strain-Stress Analysis of GMAW. *Journal of Engineering Materials and Technology*, 113:336–343, 1991.

[3] J. H. Argyris, J. Szimmat, and K. J. Willam. Computational Aspects of Welding Stress Analysis. *Computer Methods in Applied Mechanics and Engineering*, 33:635–666, 1982.

[4] H. Hibbitt and P. V. Marcal. A Numerical, Thermo-Mechanical Model for the Welding and Subsequent Loading of a Fabricated Structure. *Computers & Structures*, 3(1145-1174):1145–1174, 1973.

[5] H. J. Braudel, M. Abouaf, and J. L. Chenot. An Implicit and Incremental Formulation for the Solution of Elastoplastic Problems by the Finite Element Method. *Computers and Structures*, 22(5):801–814, 1986.

[6] P. Michaleris, D. A. Tortorelli, and C. A. Vidal. Analysis and Optimization of Weakly Coupled Thermo-Elasto-Plastic Systems with Applications to Weldment Design. *International Journal for Numerical Methods in Engineering*, 38(8):2471–2500, 1995.

[7] E. F. Rybicki and R. B. Stonesifer. Computation of Residual Stresses due to Multipass Welds in Piping Systems. *Journal of Pressure Vessel Technology*, 101:149–154, 1979.

[8] Y. Shim, Z. Feng, S. Lee, D.S. Kim, J. Jaeger, J. C. Paparitan, and C. L. Tsai. Determination of Residual Stress in Thick-Section Weldments. *Welding Journal*, 71:305s–312s, 1992.

[9] L. A. Bertram and A. R Ortega. Automated Thermomechanical Modeling of Welds Using Interface Elements for 3D Metal Deposition. In *Manuscript for Proceedings of ABAQUS User's Conference*, Oxford: Hibbit Karlsson and Sorensen Inc., 1991.

[10] J. Lubliner. *Plasticity Theory.* Macmillan Publishing Company, New York, 1st edition, 1990.

[11] R. Gunnert. *Residual Welding Stressed.* Almqvist & Wiksell, Stockholm, 1955.

[12] K. Terai. Study on Prevention of Welding Deformation in Thin-Skin Plate Structures. Technical Report 61, Kawasaki, 1978.

[13] L. P. Connor, editor. *Welding Handbook.* American Welding Society, Miami, FL, eighth edition, 1987.

[14] Ya. I. Burak, L. P. Besedina, Ya. P. Romanchuk, A. A. Kazimirov, and V. P. Morgun. Controlling the longitudinal plastic shrinkage of metal during welding. *Avt. Svarka*, 3:27–29, 1977.

[15] Ya. I. Burak, Ya. P. Romanchuk, A.A. Kazimirov, and V. P. Morgun. Selection of the optimum fields for preheating plates before welding. *Avt. Svarka*, 5:5–9, 1979.

[16] J. Goldak, A. Chakravarti, and M. Bibby. A New Finite Element Model for Welding Heat Sources. *Metallurgical Transactions B*, 15B:299–305, 1984.

[17] M. V. Deo and P. Michaleris. Mitigation of Welding induced Buckling distortion using Transient Thermal Tensioning. *Science and Technology in Welding*, 2002. To appear.

[18] VMA Engineering. *DOT User's Manual, Version 3.00.* Vanderplaats, Miura and Associates, Inc., Goleta, CA, 1992.

[19] K. Masubuchi. *Analysis of Welded Structures.* Pergamon Press, Oxford, 1980.

[20] H. Murakawa Y. Ueda X. M. Zhong. Buckling Behavior of Plates under Idealized Inherent Strain. *Transactions of JWRI*, 24(2):87–91, 1995.

[21] P. Michaleris and A. DeBiccari. Prediction of Welding Distortion. *Welding Journal*, 76(4):172–180, 1997.

[22] C.L. Tsai, S.C. Park, and W.T. Cheng. Welding Distortion of a Thin-Plate Panel Structure. *A.W.S. Welding Journal, Research Supplement*, 78:156s–165s, 1999.

[23] Y. Ueda, Y.C Kim, and M.G Yuan. A Predictive Method of Welding Residual Stress Using Source of Residual Stress (Report I) Characteristics of Inherent Strain (Source of Residual Stress). *Transactions of JWRI*, 18(1):135–141, 1989.

[24] P. Michaleris and A. DeBiccari. A Predictive Technique for Buckling Analysis of Thin Section Panels due to Welding. *Journal of Ship Production*, 12(4):269–275, 1996.

[25] P. Michaleris, Z. Feng, and G. Campbell. Evaluation of 2D and 3D FEA Models for Predicting Residual Stress and Distortion. In *Pressure Vessel and Piping Conference*. ASME, 1997.

[26] L.-E. Lindgren. Modelling for residual stresses and deformations due to welding: Knowing what isn't necessary to know. Graz, Austria, 2001. International Institute of Welding. Keynote at 6th Int. Seminar Numerical Analysis of Weldability.

[27] J. Goldak and M. Bibby. Computational Thermal Analysis of Welds: Current Status and Future Directions. In A. F. Giamei and G. J. Abbaschian, editors, *Modeling of Casting and Weldin Processes IV*, pages 153–166, Palm Coast, FL, 1988. The Minerals & Materials Society.

[28] D.F.Watt, L.Coon, M.Bibby, and C.Henwood. Coupled transient heat transfer-microstructure weld computations (part b). *Acta metall.*, 36(11):3037–3046, 1988.

[29] P. Tekriwal and J. Mazumder. Finite Element Analysis of Three-dimensional Tranient Heat Transfer in GMA Welding. *A.W.S. Welding Journal, Research Supplement*, 67:150s–156s, 1988.

[30] M. V. Deo, P. Michaleris, and J. Sun. Prediction of Buckling Distortion of Welded Structures. *Science and Technology in Welding*, 2002. To appear.

[31] A. S. Oddy, J. A. Goldak, and J. M. J. McDill. Numerical Analysis of Transformation Plasticity in 3 D Finite Element Analysis of Welds. *European Journal of Mechanics, A/Solids*, 9(3):253–263, 1990.

[32] K. J. Bathe. *Finite Element Procedures in Engineering Analysis*. Prentice-Hall, Inc., Englewood Cliffs, New Jersey, NJ, 1982.

[33] R. D. Cook, D. S. Malkus, and M. E. Plesha. *Concepts and Applications of Finite Element Analysis*. John Wiley and Sons, Inc., New York, NY, 1988.

[34] C. Farhat and F.X. Roux. A method of finite element tearing and interconnecting and its parallel solution algorithm. *International Journal for Numerical Methods in Engineering*, 32:1205–1227, 1991.

[35] C. Farhat and J. Mandel. The two-level FETI method for static and dynamic plate problems Part I: An optimal iterative solver for biharmonic systems. *Computer Methods in Applied Mechanics and Engineering*, 155:129–152, 1998.

[36] C. Farhat, K. Pierson, and M. Lesoinne. The Second Generation of FETI Methods and their Application to the Parallel Solution of Large-Scale Linear and Geometrically Nonlinear Structural Analysis Problems. *Computer Methods in Applied Mechanics and Engineering*, 184:333–374, 2000.

[37] C. Farhat, M. Lesoinne, and K. Pierson. A Scalable Dual-Primal Domain Decomposition Method. *Numerical Linear Algebra with Applications*, 7:687–714, 2000.

[38] C. Farhat, M. Lesoinne, P. LeTallec, K. Pierson, and D. Rixen. FETI-DP: a dual-primal unified FETI method - part I: A faster alternative to the two-level FETI method. *International Journal for Numerical Methods in Engineering*, 50:1523–1544, 2001.

Contract Information

Contract Number	N000140010741
Title of Research	Development of a Computer Aided Weld Design Tool
Principal Investigator	Panagiotis (Pan) Michaleris
Organization	The Pennsylvania State University

Technical Section

1 Technical Objectives

The objective of this project is to develop a computer aided weld design tool for a computer integrated design and manufacturing system.

The weld design tool will allow for the determination of appropriate welding conditions and if needed auxiliary heating for a specific structural design such that welding distortion is within tolerance. The database will be integrated with Computer Aided Production Engineering (CAPE) software.

The project contributes to a collaborative effort by Maglev Inc and other Universities entitled "Demonstration of Computer Aided Manufactuting Techniques for the Precision Fabrication of Large Steel Curved Plate Beam Components for Shipbuilding and Other Industries."

2 Technical Approach

The proposed program is organized in the following five tasks:

1. Identification of structural features that welding distortion
2. Inverse method and database architecture
3. Generation of a database
4. Integration with computer aided production engineering software
5. Modifications and refinement using production tests

3 Progress

3.1 Identification of structural features that welding distortion

Welding, among all mechanical joining processes, has been employed at an increasing rate for its advantages in design flexibility, cost savings, reduced overall weight and enhanced structural

performance. However, welding induces various types of distortions as discussed in detail by Masubuchi [1]. To access the effects of welding on structure efficiently, and hence in turn to implement various distortion mitigation techniques, a validated method for predicting welding induced distortion is necessary.

Thinner section components made of higher strength steels are being commonly utilized in shipbuilding, railroad and aerospace industries in fabricating large structures to achieve reduction in overall weight and more controllable manufacturing. However, for structures made of relatively thin components, welding can introduce significant buckling distortion which causes loss of dimensional control, structural integrity and increased fabrication costs due to poor fit-up between panels. A predictive analysis technique can determine the susceptibility of a particular design to buckling distortion. Further, a predictive analysis tool can assist in the selection of geometry and welding conditions that will induce minimum distortion. Flame straightening is the commonly used technique to correct the out-of-plane distortion resulting from welding processes, but this is an inaccurate, labor intensive and costly process. Also it is rather a corrective action after the damage is done and not a preventive measure which is generally desired in engineering processes.

Finite element techniques have been used in the prediction of welding residual stress and distortion for more than two decades. Due to the nature of the process, additional complexities are involved in the FEA of welding compared to traditional mechanics, such as temperature and history dependent material properties; high gradients of temperature, stress and strain fields with respect to both time and spatial coordinates; large deformations in thin structures and phase transformation and creep phenomena.

Earlier studies of welding accounted for the non-linearities due to temperature dependent material properties and plastic deformations [2, 3, 4]. The majority of those analyses were limited to two-dimensions on the plane perpendicular to the welding direction, but good correlations have been observed between the numerical predictions and experimental results [5, 6, 7, 8], and especially for residual stress predictions, 2-D models provided accurate estimations comparable to 3-D analyses, since the stress field exhibits a fairly uniform distribution through the length of the work-piece. Argyris et. al. [5] computed the thermo-mechanical response using 2-D models in a staggered solution strategy to combine and integrate the thermal and mechanical computational steps. Rybicki et. al. [6] performed thermo-elasto-plastic analysis on a 2-D axisymmetric finite element model for a two-pass girth-butt welded pipe problem, and verified the numerical results with the experimentally obtained temperature history and residual stress distributions. Papazoglu and Masubuchi [7] solved the multipass GMAW process problem by performing uncoupled 2-D heat transfer and stress-strain analyses, incorporating the phase transformation strains.

2-D models, as mentioned above, have been particularly useful with their high efficiency and accuracy in determining the solution in the analysis plane and reduced computational requirements. However, for welding practices where tack welding or fixturing allow out-of-plane movement 2-D analyses may not be accurate, particularly, in distortion predictions [9]. Furthermore, longitudinal heat transfer and instability aspects, and end effects (i.e. due to initiation and termination of the heat source) cannot be realized in two dimensional formulations.

Most of the currently performed welding simulations, both 2-D and 3-D, are based on small deformation assumption and are limited to simpler structures and weld geometries (e.g. butt joints)

or focusing only to the heat affected zones, ignoring the surrounding structure. A small deformation analysis assumes infinitesimal displacements and loads being applied to the undeformed geometry. The interaction between the weld zone and the structure is effective on the accumulated distortion, and large deformation modes in unrestrained structures may not be captured with this type of analysis [9], [10]. Brown and Song [9] have performed 2-D axisymmetric and 3-D weld simulations of a ring stiffened cylinder structure, and concluded that 2-D analysis overestimated the rotation of the ring during the heating segment, and it was very sensitive to model modifications, such as joint clearance and location of constraints. Michaleris et. al. [10] studied the effects of the restraints and the solidified portions of the weld on the residual stress and distortion profiles by comparing the performance of 2-D and 3-D weld simulations.

Oddy et. al. [11] examined the butt welding of a bar via 3-D FEM, and computed the temperature, strain and stress fields. Tekriwal and Mazumder [12, 13] simulated thermal and elasto-plastic response of the butt-welded plates through 3-D models, considering filler material addition. Multi-pass welding simulation of plates and experimental validation have been addressed in [14, 15].

Welding-induced buckling of thin-walled structures has been investigated in greater detail by [16, 17, 18]. Ueda et. al. [16, 19] presented a methodology to determine the buckling behavior of plates by large deformation elastic FEA and employing inherent strain distributions. Michaleris et. al. [17, 20] developed a predictive buckling analysis technique for thin section panels, combining decoupled weld process simulations and eigenvalue buckling analyses. Tsai et. al.[18] studied the distortion mechanisms and the effect of welding sequence on panel distortion.

For the welding practices where tack welds or fixturing are used to restrict the movement of the welded parts, the structural response may be evaluated by means of decoupled 2-D welding and 3-D buckling simulations. When mechanical fixturing on the structure prevents the longitudinal shrinkage during welding, the out-of-plane structural behavior doesn't have influence on the in-plane welding response, and buckling is only observed after the restraints are removed and the structure cools down. Exploiting this fact, Michaleris et. al. [17] proposed the aforementioned buckling prediction technique with uncoupled weld simulation and structural buckling analyses. They expressed the residual stress profile from the 2-D welding simulations as buckling stress on the 3-D structural model. This approach is analogous to the work by Ueda et. al. [19], where the concept of inherent strain is used to generate the welding residual stresses by applying a prescribed thermal strain field using empirical methods. In the former study, however, residual stresses are calculated with weld process simulations, which provides improved estimations for buckling analysis compared to empirically determining the residual stress.

Phase transformations and transformation plasticity have also been incorporated in the analysis as recent developments [11, 21, 22]. The primary objective there is to more accurately model the residual stress distribution, microstructure and local distortion in the area immediately adjacent to the weld.

In this work the decoupled 2-D and 3-D finite element analysis technique by Michaleris et. al. [20, 17] is applied to evaluate welding-induced buckling of the welded panels. Effects of the following process and design parameters are investigated:

3

- panel cross-section (panel thickness),
- panel size,
- welding heat input,

3.1.1 Analysis Approach - Modelling the Welding Distortion

Following the work of Michaleris et. al. [20, 17], the response of welded panels is evaluated in two steps by combining two-dimensional welding simulations with three-dimensional structural analyses in a decoupled approach.

<u>2-D Thermo-mechanical Weld Simulation :</u>

A two dimensional thermo-elasto-plastic analysis is performed to determine the angular distortions, residual stresses, and plastic strain fields during the welding process ignoring the structural response. Residual stresses are caused by the negative plastic strains resulting from the welding thermal cycle.

<u>3-D Eigenvalue Analysis :</u>

The buckling distortion and critical buckling stresses are consequently determined by an eigenvalue analysis applying the, mostly uniform and compressive, longitudinal plastic strain field of the 2-D weld model on the 3-D structural model as equivalent load.

A constant, negative thermal load is applied at the weld region to introduce the effects of welding into the 3-D structure. Thermal loading is used rather than mapping the plastic strain field, which would require a complex analysis procedure. An eigenvalue analysis is performed to determine the critical residual stresses and buckling distortions.

Welding Simulation

The welding simulation involves a thermal and a mechanical analysis. The effect of mechanical response is assumed to be negligible on the thermal behavior, thus the temperature field is solved independently from the mechanical solution. To determine the temperature history profile, a non-linear, transient heat-flow finite element analysis is performed on the plane perpendicular to the welding direction.

<u>Thermal Analysis</u>

4

The numerical implementation of the history dependent (transient) heat transfer problem involves an incremental scheme with several small time increments. The solution at a given time increment is obtained by using the solution at the previous time increment as an initial condition. This problem is addressed in detail in references [3, 23, 12].

The governing energy balance equation for transient heat transfer analysis is given as follows,

$$\rho C_p \frac{dT}{dt}(\mathbf{r}, t) = -\nabla_{\mathbf{r}} \cdot \mathbf{q}(\mathbf{r}, t) + Q(\mathbf{r}, t) \qquad \text{in the entire volume } V_{\mathbf{r}} \text{ of the material} \qquad (1)$$

where ρ is the density of the body ($[7,820 kg/m^3]$), C_p is the specific heat capacity, T is the temperature ($[^oC]$), $\mathbf{q}$ is the heat flux vector, Q is the internal heat generation rate, t is the time, $\mathbf{r}$ is the coordinate in the reference configuration and $\nabla_{\mathbf{r}}$ is the spatial gradient operator. Material properties for medium carbon steel (A36) are used in this study (Figure 1).
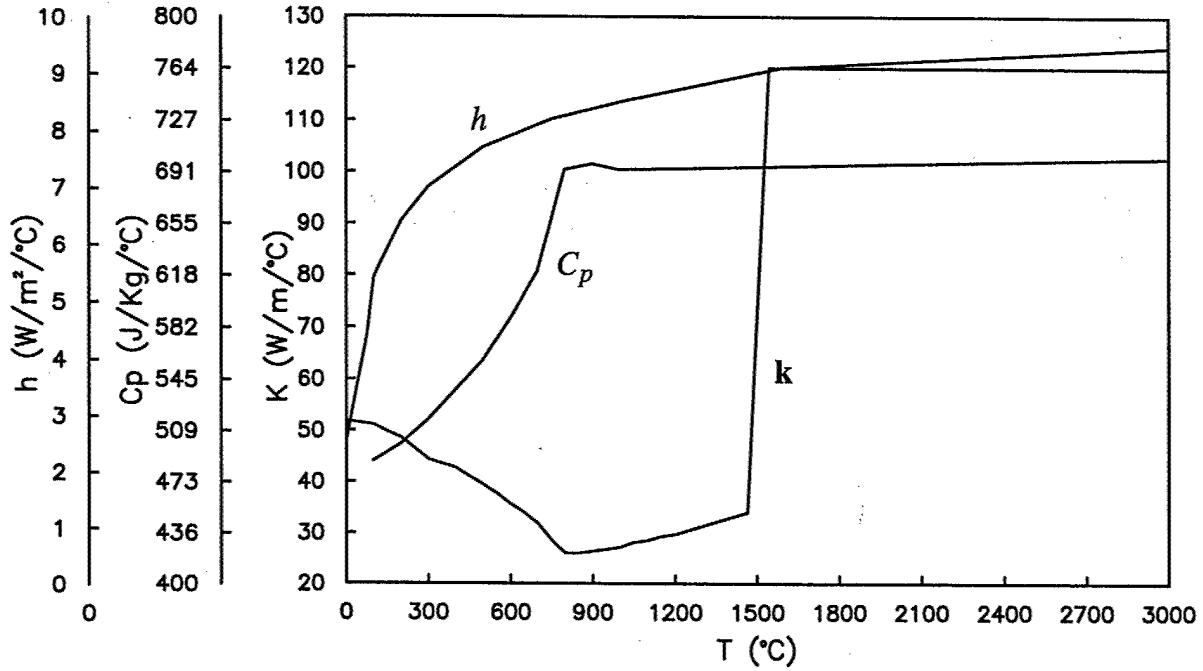
Figure 1: Conductivity (k), specific heat (C_p), and air convection (h) for A36.

The nonlinear isotropic Fourier heat flux constitutive relation is enforced; using the temperature-dependent thermal conductivity, $\mathbf{k}$ ($[\frac{W}{^oC mm^2}]$),

$$\mathbf{q} = -\mathbf{k}\nabla_{\mathbf{r}}T \qquad\qquad [W/mm^2] \qquad (2)$$

Convection boundary conditions are assigned for all free surfaces. The internal heat generation rate by the welding torch, modeled with a "double ellipsoid" heat source model [24], is given as,

$$Q = \frac{6\sqrt{3}Q_b(\eta)f}{abc\pi\sqrt{\pi}} \, e^{-[\frac{3x^2}{a^2}+\frac{3y^2}{b^2}+\frac{3(z+vt)^2}{c^2}]} \qquad [W/mm^3] \qquad (3)$$

5

where Q_b is the welding heat input; η is the welding efficiency, x, y, and z are the local coordinates of the double ellipsoid model aligned with the weld fillet; a is the weld width; b is the weld penetration; $c = 4a$ is the weld ellipsoid length, and $f = 0.6$ when the torch is behind the analysis plane, and $f = 1.4$ after the torch passes the analysis plane; v is the torch travel speed; and t is time.

Elasto-plastic Mechanical Analysis

The subsequent history dependent stress analysis is performed by modelling the stress problem as a quasi-static process in a Lagrangian frame. This problem has been covered by several investigators [5, 15, 4, 13, 11]. Similar to the heat transfer analysis, the numerical implementation of the quasi-static analysis involves an incremental scheme with several small static increments. The solution at a given time interval is obtained by using the solution at the previous time increment as an initial condition.

The temperature values solved for in the previous thermal analysis are imported to the mechanical analysis as loading. Generalized plane-strain conditions are assumed to account for the out-of-plane expansion in the structure. The longitudinal (out-of-plane) strain is assumed to vary linearly with x- and y- coordinates in the analysis plane:

$$\epsilon_z = e - x\phi_y + y\phi_x \tag{4}$$

where e is the z-component of the strain at the coordinate origin and the constants ϕ_x and ϕ_y represent the strain variations in the y and x axes, respectively.

The stress equilibrium equation is given by,

$$\nabla_r \sigma(\mathbf{r}, t) + \mathbf{b}(\mathbf{r}, t) = 0 \qquad \text{in } V_r \tag{5}$$

where σ is the stress, $\mathbf{b}$ the body force, and t is time. The mechanical constitutive law is :

$$\dot{\sigma} = \mathbf{C} \left(\dot{\epsilon} - \dot{\epsilon}_p - \dot{\epsilon}_t \right) \tag{6}$$

$$\dot{\epsilon}_p = \dot{\epsilon}_q \cdot \mathbf{a} \left(\sigma, \epsilon_q, \mathbf{T} \right) \tag{7}$$

$$f = \sigma_e - \sigma_y \leq 0 \tag{8}$$

where $\mathbf{T}$ is temperature, $\mathbf{C}$ is the material stiffness tensor, $\mathbf{a}$ is the plastic flow vector, ϵ, ϵ_p and ϵ_t are the total, plastic and thermal strains and ϵ_q is the equivalent plastic strain. In Equation (8), f is the yield function, σ_e is the Von Misses stress, and σ_y is the yield stress. Active yielding occurs when $f = 0$. Figures 2 and 3 illustrated the mechanical material properties assumed for A36.

Structural Analysis

The longitudinal residual stress distribution (σ_r) computed in the 2-D analyses are compared to the critical buckling stresses (σ_{cr}) of the structure from the 3-D structural analysis to determine if the structure will buckle.
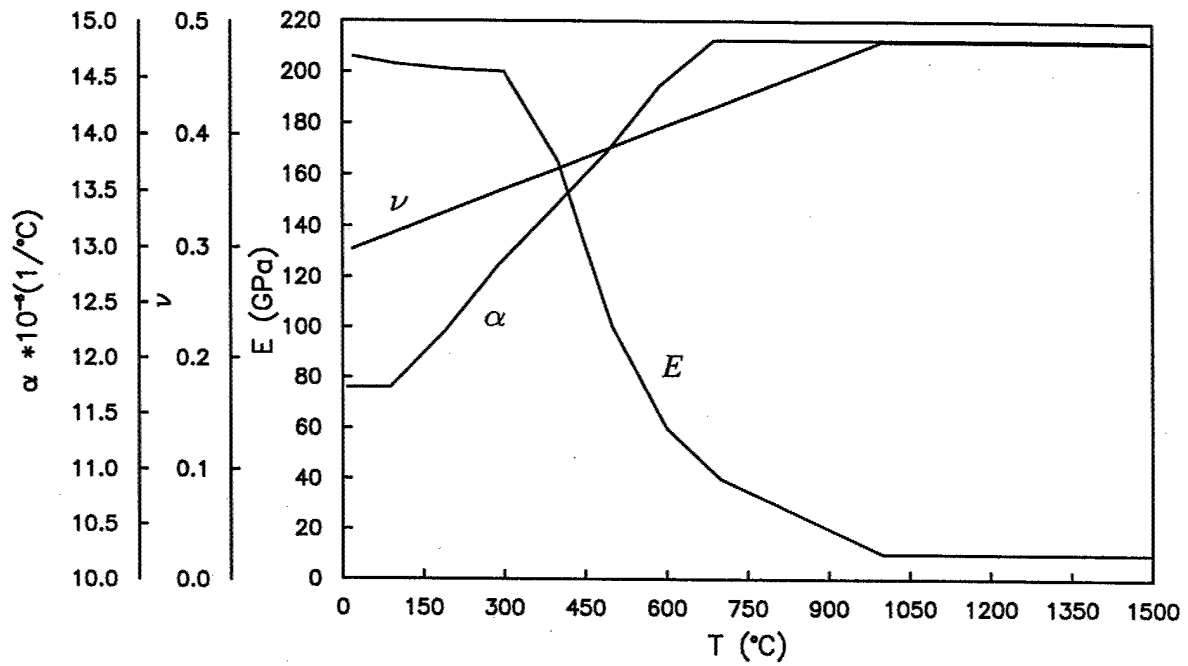
6

Figure 2: Elastic modulus (E), Young's modulus (ν), and thermal expansion coefficient (α) for A36.
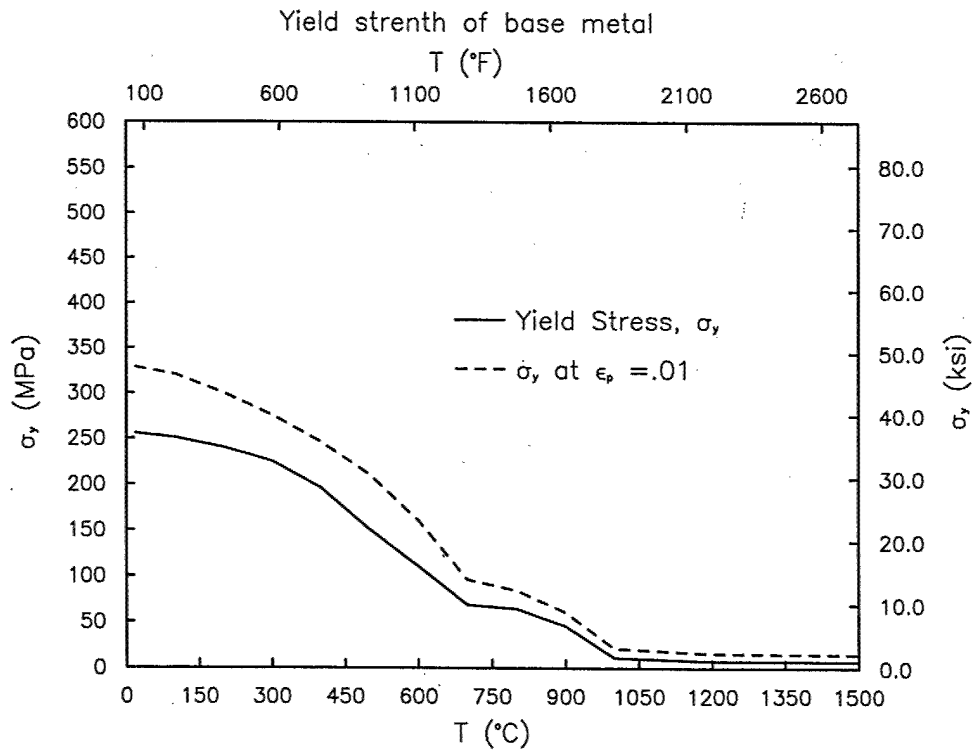

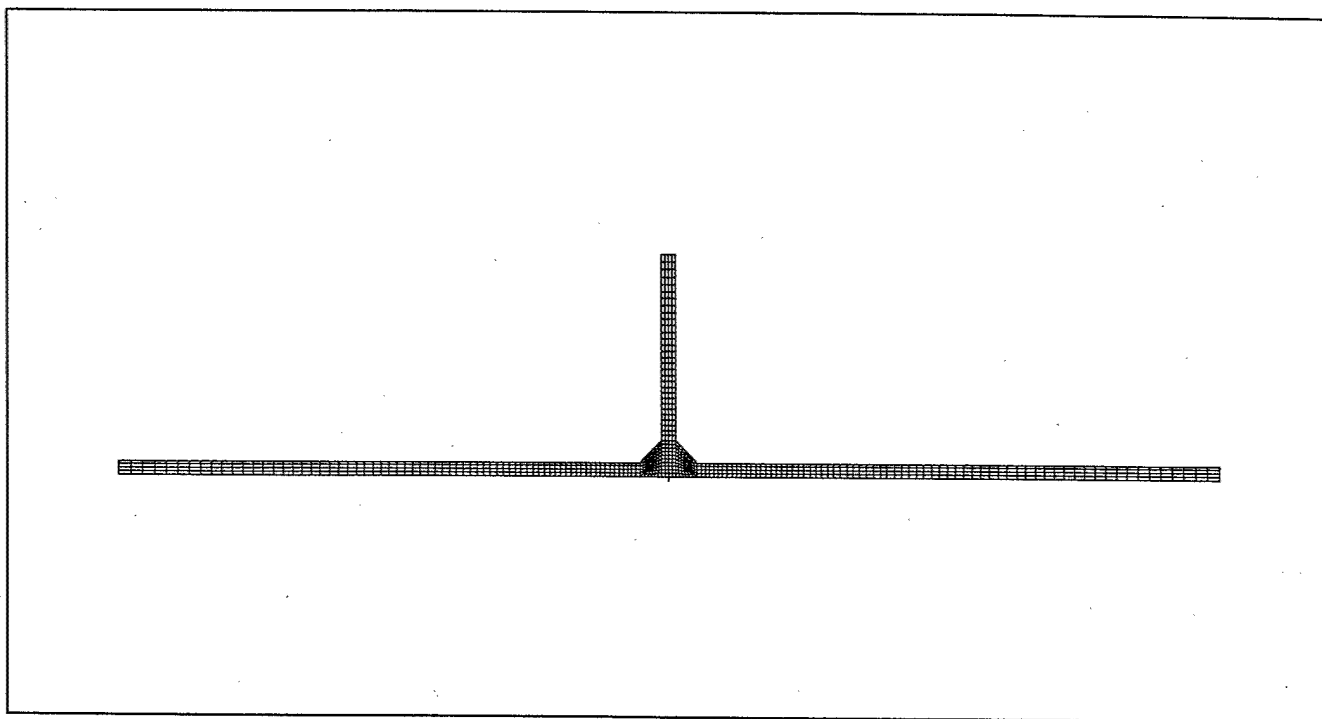Figure 3: Yield strength for A36.

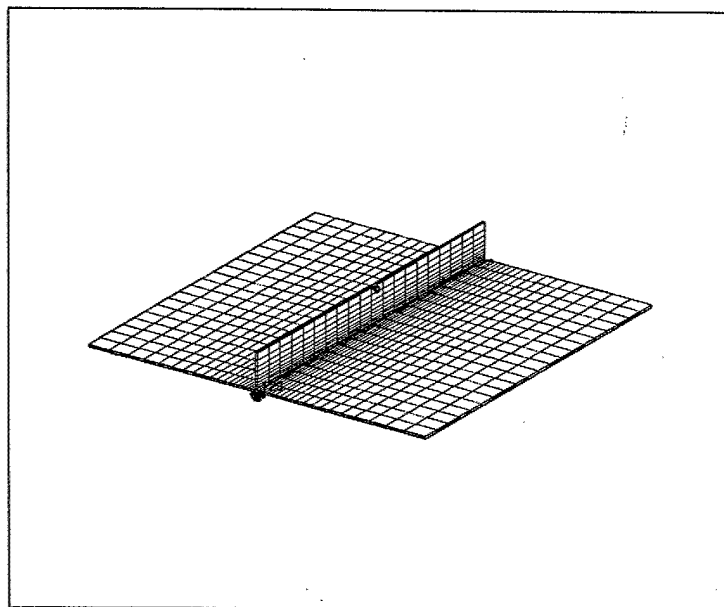Figure 4: FEA mesh for 2-D welding process analysis

Figure 5: FEA mesh for 3-D buckling analysis

The structural analysis involves elastic eigenvalue analysis. Incremental large deformation analyses may also be performed to determine the onset of buckling, buckling and post buckling stages in response to increasing stress, but they are computationally intensive and are usually used for validating the predictive methodology [17].

3-D Eigenvalue Buckling Analysis:

The elastic instability problem is defined as an eigenvalue problem as follows

$$det\ (\ \mathbf{K} + \lambda \mathbf{K_G}\ ) = \mathbf{0} \tag{9}$$

where $\mathbf{K}$ and $\mathbf{K_G}$ are the linear and non-linear strain stiffness matrices, and λ is the eigenvalue.

A 3-D eigenvalue analysis is performed on the structural model with a unit negative thermal load applied in the weld region $(T = -1.0)$ to model the uniform compressive longitudinal plastic strain field occurring in welding. The eigenvalues (λ_i) represent the multipliers (scaling factors) which result in the critical buckling stress field $(\sigma_{cr})_i$ when multiplied with the stress field resulting from the unit thermal load (σ_L). Equation (10) shows the computation of the critical residual stress distribution at the plate midspan.

$$(\sigma_{cr})_i = \lambda_i \cdot \sigma_L \qquad \text{[MPa]} \tag{10}$$

The buckling analyses may yield negative eigenvalues, which often cannot be explained by "physical" behavior. Those situations can be avoided by applying enough preload T_p, to load the structure just below the buckling load before performing the eigenvalue analysis. In such a case, the critical buckling stress in Equation (10) is determined as

$$(\sigma_{cr})_i = (\ \lambda_i + |\ T_p\ |\ ) \cdot \sigma_L \qquad \text{[MPa]} \tag{11}$$

Buckling distortion is determined from the eigenvectors (mode shapes) of the structure. The structure may buckle in any of the modes with critical stresses lower than the residual stress field due to welding. It will prefer to buckle with the permissible buckling mode having the lowest critical stress. The permissibility of the modes are determined by the constraints on the structure. If certain buckling modes are suppressed by the mechanical fixturing applied, the structure will tend to buckle the next available (higher) mode. The weight of the structure might have an influence of causing even higher buckling modes.

3.1.2 Verification

Experimental Setup

The predictive buckling analysis approach taken in this work is verified with the experiments. The panels of the same size as modelled are used. All other welding conditions like heat input and boundary conditions are also used same as in the Finite Element Model.

Three different panels with appropriate welding conditions are used in this experiment as listed in Table 1. The welding setup consists of two welding guns on either side of the stiffener plate. The guns are 3.5" offset from each other with one gun following the other. This is shown in the Figure 6. Constant Voltage Metal Inert Gas welding is carried out. Welding electrode of 0.045" Dia. is used with a mixture of 75/25 Argon and Carbon Dioxide shielding gas. The welding conditions are set to give short circuiting transfer mode of the welding.
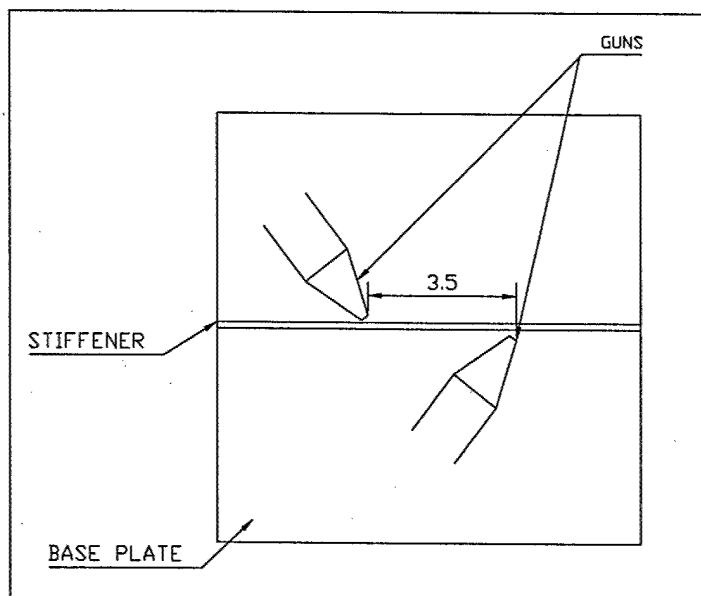

Figure 6: Experimental Arrangement

A linear motion device is used for getting constant velocity of welding and also to maintain a constant stickout through the weld. The welding gun speed for all welds is maintained at 15 Inches per minute and an electrical stickout of 1/2". The gas flow of 35 cubic Feet per hour is used for shielding. Drag angle of 15 degrees is used between the gun and the vertical plane.

The stiffeners are tack welded to the base plate to make the T-shaped panels ready for the welding. The vertical stiffener plate is held horizontally with screws and the rammed down with pneumatic cylinders. The panel is supported by a copper plate during welding for rapid post-welding cooling and also to avoid welding of specimen to the base iron table. The edges of the specimen are let loose and they are not restricted in any degree of freedom. Welding is carried out on all the panels shown in Figures 7 and 8 with the respective welding conditions listed in Table 1. No water or forced air cooling of panel is done after the welding is complete. The panel is taken out once it is cooled down and the distortion is examined.

The panel is fabricated by joining a small stiffener plate to a large plate longitudinally in a T-joint configuration. Three different panel geometries are considered, as illustrated in Table 1.
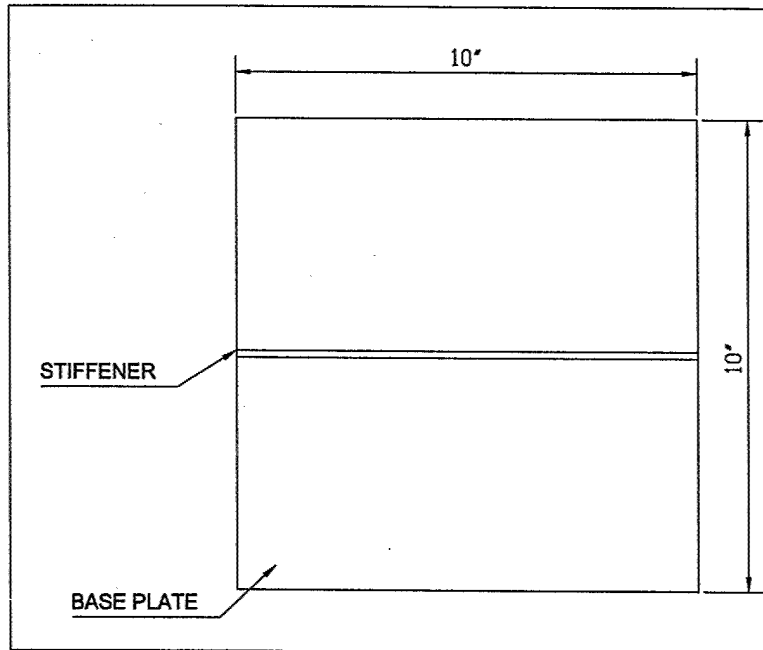
10

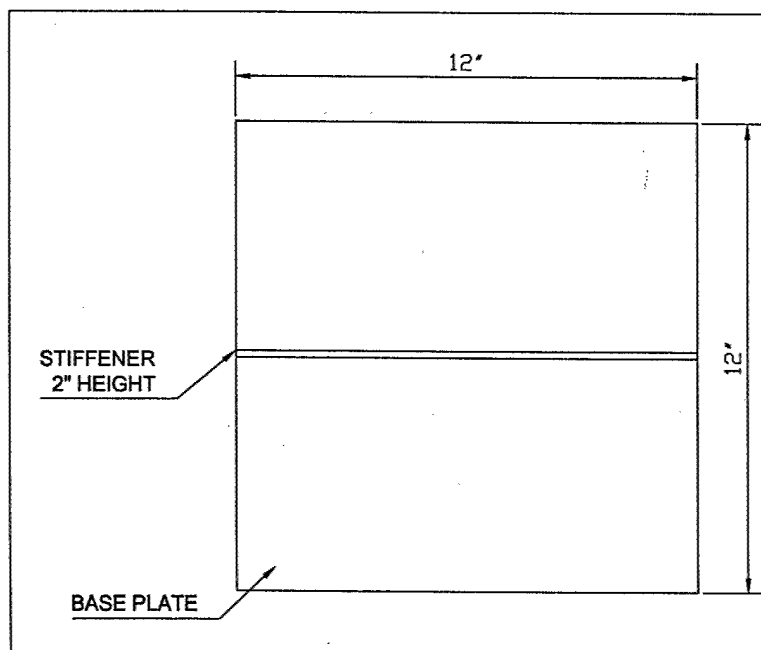Figure 7: 10" X 10" Panel in 1/16" and 1/8" thickness

Figure 8: 12" X 12" Panel in 1/8" thickness

11

Case	Size in.	Thickness in.	Volts	Amps	Travel Speed in./min	Wire feed in./min
1	10x10	1/16	17.8	68	15	75
2	10x10	1/8	21.4	167	15	180
3	12x12	1/8	21.4	167	15	180

Table 1: Weld Parameters

The fillet welds of size 1/5 in. and 1/16 in. on thick and thin plates are performed respectively on both sides with dual-torches by gas metal arc (GMAW). The effect of geometry and process parameters are studied.

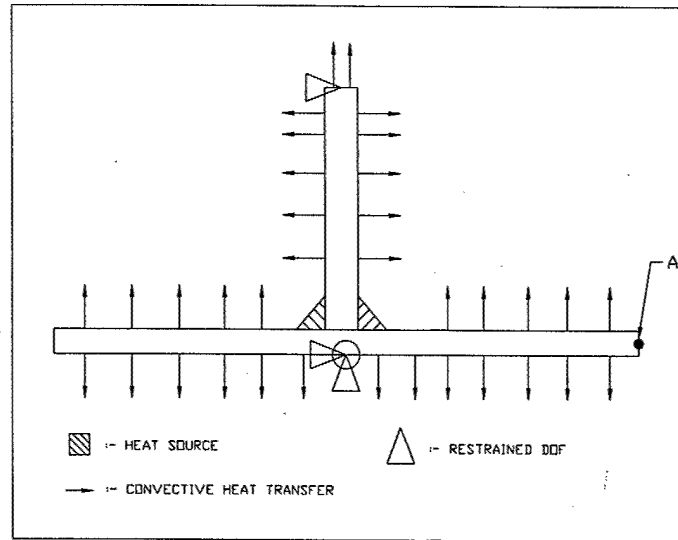### 3.1.3 Numerical Implementation

Figure 9: Boundary Conditions for 2-D welding simulation models

The boundary conditions used in the model for the analysis are shown in the Figure 9. This shows the corners where fillet weld is done as heat sources. All the free surfaces are taken as the convective surfaces. The bottom center node is restricted in all degrees of freedom and the top center node of the stiffener plate is restricted in X direction.

The Finite Element solutions are performed using a SMP Fortran90 finite element code developed in-house for the 2-D models and ABAQUS software is used for the 3-D models. The implementation details pertaining to those problems like the type of elements, boundary and loading conditions are presented to allow convenient reproduction.

2-D Welding Simulation

12

The 2-D finite element mesh used in the heat transfer and mechanical analysis of the panel is illustrated in Figure 4. The model is made up of heat conduction, quadratic(8 node), quadrilateral elements. The quasi-static mechanical problem, following the heat transfer analysis, is discretized into a generalized plane strain finite element model. Model for case 1 uses 1123 nodes and 316 elements. Models for case 2 and case 3 use 2973 nodes and 3253 nodes respectively and 866 elements and 946 elements respectively.

To model the restriction of the supporting plate, the downward motion of the plates should be restrained. This is implemented by placing two nonlinear spring elements at the two outermost nodes of the 2-D model, to exert high reaction forces to resist the downward motion. The spring element stiffness is defined as a nonlinear function of the y-displacement as follows,

$$k = \begin{cases} 10^6 & y < 0 \\ 0 & y \geq 0 \end{cases} \quad [\text{N/mm}] \quad (12)$$

3-D Buckling Analysis

The 3-D continuum finite element models are developed to calculate critical buckling loads λ. 2-D generalized plain strain models are developed to compute the stress resulting from unit thermal load σ_L.

All 3-D models contain 1020 Hex 8 elements, and a total of 2184 nodes. The first 2-D generalized plain strain models contains 104 Quad 8 elements and 423 nodes, the second contains 216 Quad 8 elements and 767 nodes, and the third contains 216 Quad 8 elements and 767 nodes.

Unit thermal load is added along the crossing of the flanges and the stiffener, no preload is added. The 3-D finite element mesh of the small stiffener is illustrated in Figure 5.

3.1.4 Results

Numerical Results

2-D Analysis

After running the welding simulation for 2-D model, the distortion, Cauchy's stress and plastic strain in longitudinal direction are obtained. Figure 10 shows the distribution of residual stresses in Z direction after the 2-D analysis of welding for case 1. The stresses are tensile in the weld zone
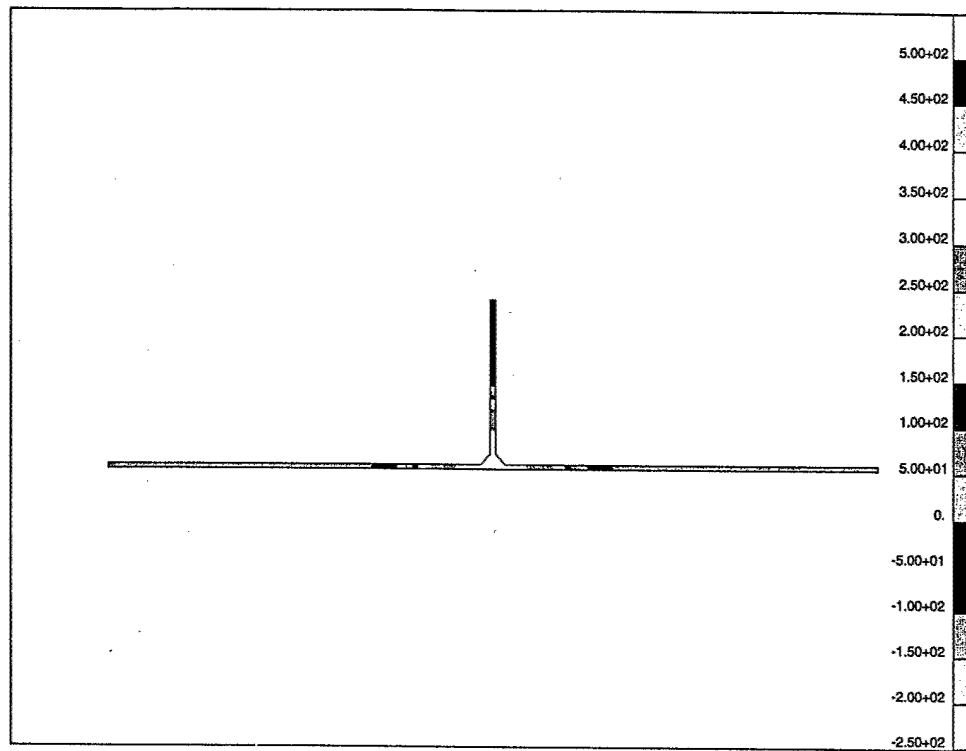
13

Figure 10: Residual Stress obtained from 2-D analysis for case 1

Case	Size in.	Thickness in.	Heat input kJ/in.	s_{res} MPa
1	10x10	1/16	4.8	-127
2	10x10	1/8	14.3	-190
3	12x12	1/8	14.3	-156

Table 2: Analytical Residual stress using 2-D analysis

and in heat affected zone. However, away from the weld zone, the stress changes the sign from tensile to compressive. Figures 11 and 12 show the plastic strain and angular distortion for case 1. Plastic strain also changes sign farther from the weld zone. Spring elements at the ends of the panel do not allow downward distortion thus correctly modelling the base support plate.

Table 2 lists the values of maximum compressive stress in all the panels. The residual stress in the 10" X 10" thin (1/16") panel is the minimum and that in the 10" X 10" thick (1/8") panel is the maximum. The table also lists the heat input that was used to cause that residual stress. A smaller weld is needed to weld the thin panel (1/16" thickness). And more heat input will result in a burn-through of the specimen. This is the maximum heat input that can be safely induced in a double fillet weld configuration with a satisfactory fillet weld and without getting burn-through. On the other hand, in the thick panel, welding heat is dictated by the satisfactory fillet weld. Both the geometries of the thick panel use the same heat input.
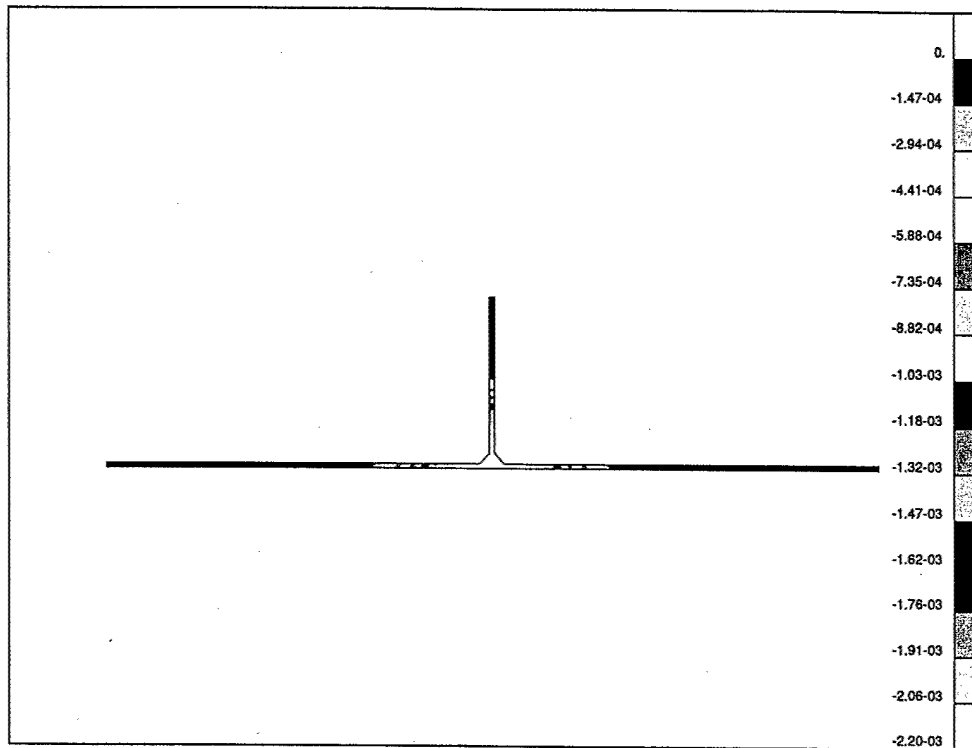
14

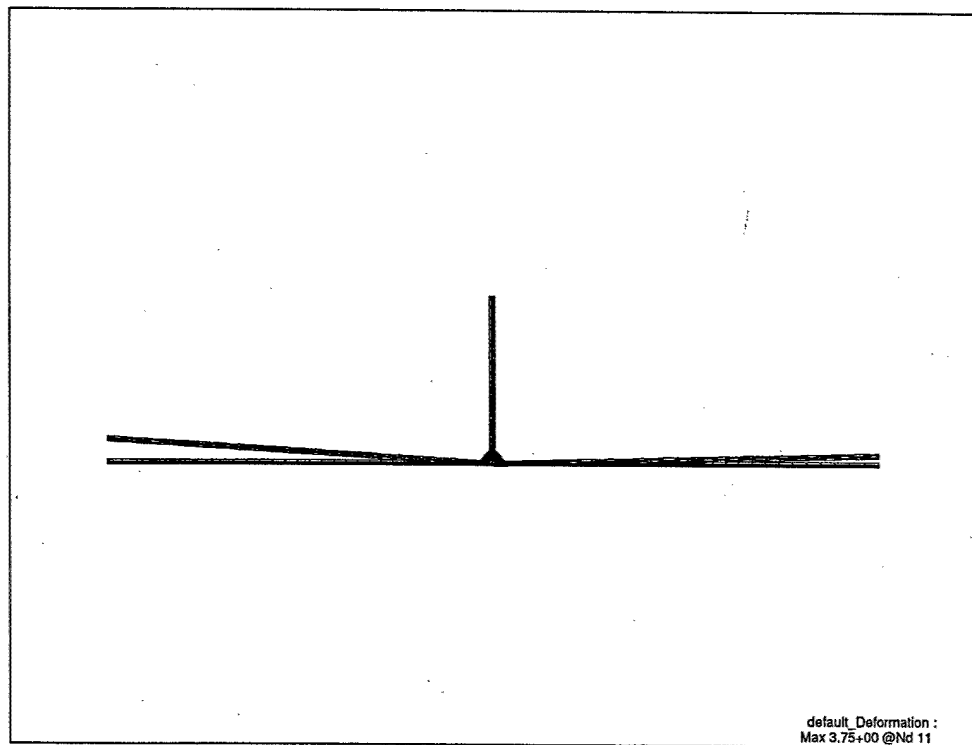Figure 11: Plastic Strain obtained from 2-D analysis for case 1

Figure 12: Angular Distortion obtained from 2-D analysis for case 1

Case	Size in.	Thickness in.	λ	σ_L MPa	s_{cr} MPa
1	10x10	1/16	0.025113	-1803	-45
2	10x10	1/8	0.060468	-3162	-191
3	12x12	1/8	0.049021	-2729	-134

Table 3: Critical stress using 3-D analysis
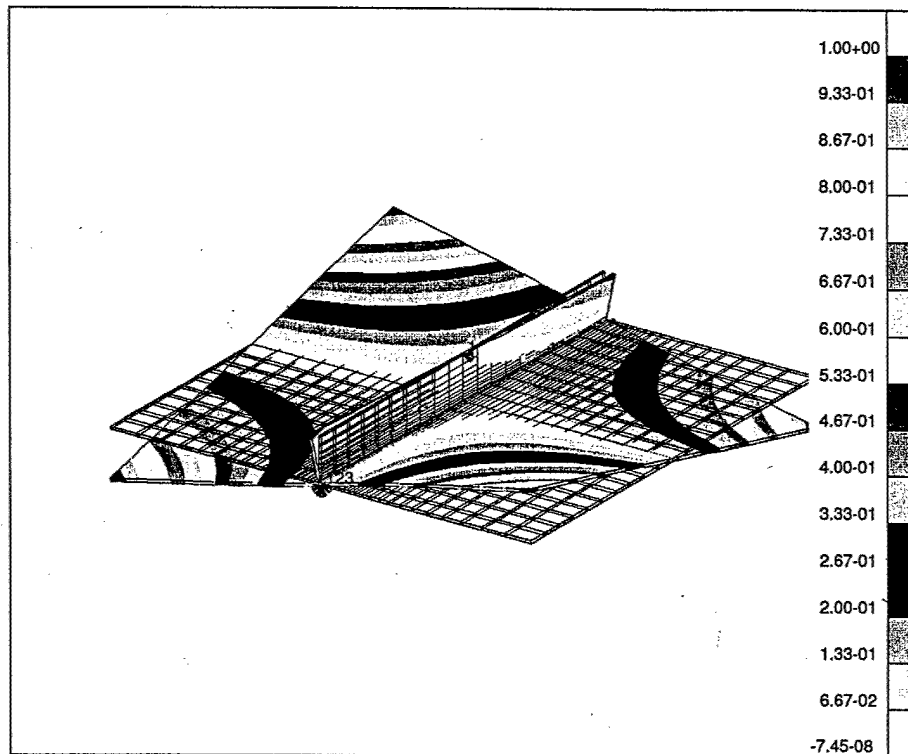
3-D Analysis

Figure 13: Buckling Distortion obtained by 3-D analysis

The results of the 3-D eigenvalue buckling analysis are presented in Table 3. The critical and residual stresses for case 1 are -45 MPa and -127 MPa respectively. This implies that there will be buckling of panel in Case 1. Similarly, -134 MPa and -156 MPa are the critical and residual stress values for case 3. So this panel is also going to buckle. However in case 2, critical stress is -191 MPa and residual stress is -190 MPa. And hence the panel in Case 2 will not buckle.

Experimental Results

The experiments are carried out as per the welding conditions described in Table 1. All the

16

Case	Size in.	Thickness in.	Heat input kJ/in.	s_{res} MPa	s_{cr} MPa	Buckling Predicted	Whether buckled
1	10x10	1/16	4.8	-127	-45	Yes	Yes
2	10x10	3/16	14.3	-190	-191	No	No
3	12x12	3/16	14.3	-156	-134	Yes	Yes

Table 4: Comparison Table for Analytical and experimental results

three panels are welded and let cool down. After the panels are cooled down, the distortion is examined. The 10" X 10" X 1/16" (case 1) panel shows clear buckling distortion. This is shown in Figure 14. However, 10" X 10" X 1/8" (case 2) and 12" X 12" X 1/8" (case 3) panels behave differently with the same welding conditions and hence the heat input. The case 2 panel shows angular distortion and there is no buckling distortion in that panel as shown in Figure 15. On the other hand, case 3 panel shows buckling distortion clearly. This buckling can be seen in Figure 16.
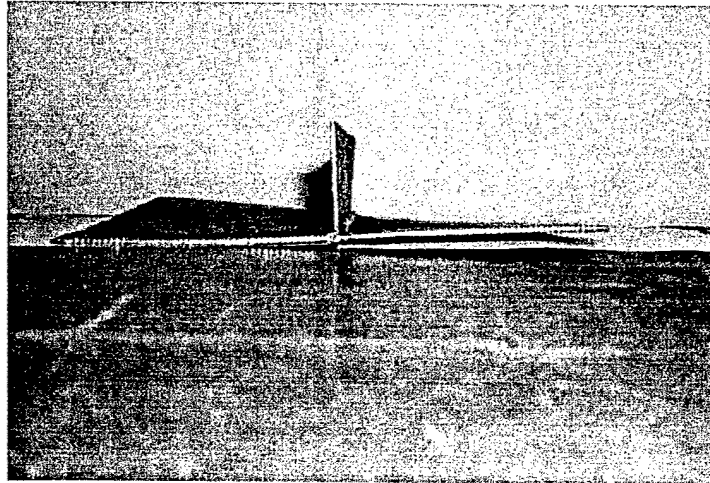

Figure 14: Buckling Distortion in case 1

A table to compare 2-D and 3-D analytical results with experimental results is drawn. Table 4 shows the successful validation of analytical results. The experimental results are in agreement with the corresponding analytical results. In the cases where buckling is predicted analytically, we can see the occurrence of buckling in the experimental results.

3.2 Inverse method and database architecture

Sensitivity analysis has been developed for the eigenvalue buckling problem. The derivative of a panel's critical buckling strength with respect to structural parameters such as panel thickness and size is computed in numerically consistent and efficient manner. This section presents the mathematical formulations and verification performed on a small example.
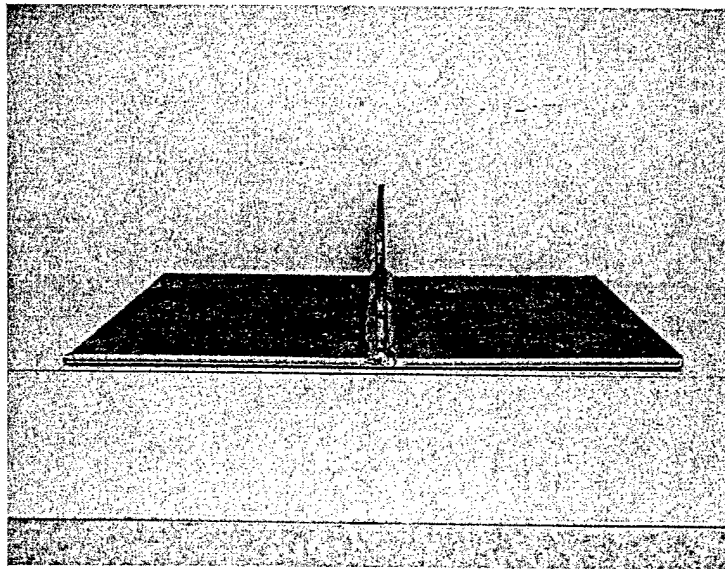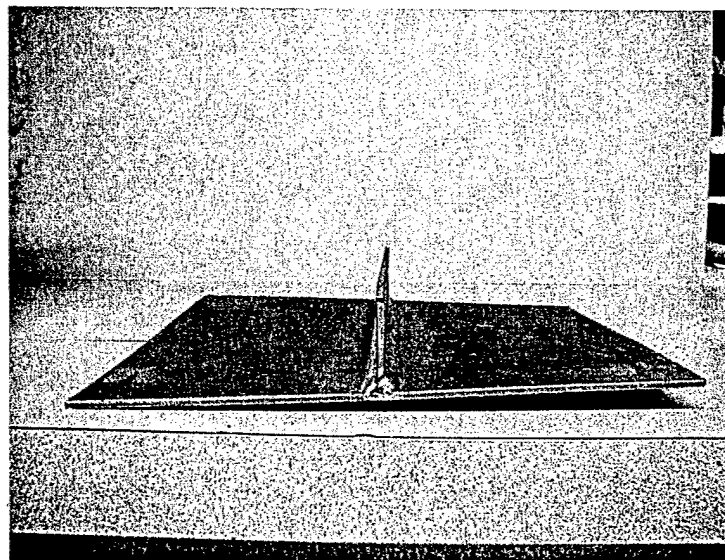
17

Figure 15: Angular Distortion in Case 2

Figure 16: Buckling Distortion in Case 3

18

3.2.1 Mathematic formulation

Buckling equations

Buckling analysis can be expressed as a generalized eigenvalue problem as follows [25, 26]:

$$[\mathbf{K} - \lambda_i \mathbf{K}_s]\phi_i = 0 \tag{13}$$

where $\mathbf{K}$ is linear stiffness matrix, which is symmetric positive definite. $\mathbf{K}_s$ is stress stiffness matrix with unit load, which is symmetric, but not necessary positive definite. λ is eigenvalue, which represents the critical buckling load, and ϕ is eigenvector, which corresponds to buckling mode.

The detailed formulation of $\mathbf{K}$ and $\mathbf{K}_s$ are given below:

$$\mathbf{K} = \int \mathbf{B}^{\mathbf{T}}\mathbf{EB}dV \qquad \epsilon = \mathbf{BU} \qquad \mathbf{U} = \mathbf{Nu} \tag{14}$$

$$\mathbf{K}_s^{ij} = \int \Delta\sigma : [(\frac{\partial \mathbf{N}^i}{\partial \mathbf{x}})^T \cdot \frac{\partial \mathbf{N}^j}{\partial \mathbf{x}} - 2(\frac{\partial \mathbf{N}^j}{\partial \mathbf{x}})_{sym} \cdot (\frac{\partial \mathbf{N}^i}{\partial \mathbf{x}})_{sym}]dV$$

$$- \int \mathbf{N}^i \cdot \frac{\partial \Delta\mathbf{p}}{\partial u^j}dS - \int \mathbf{N}^i \cdot \frac{\partial \Delta\mathbf{b}}{\partial u^j}dV \tag{15}$$

where $\mathbf{N}$ is the matrix of shape function, $\mathbf{E}$ is the matrix of Young's modula, and $\mathbf{B}$ is the derivative of matrix $\mathbf{N}$, $\mathbf{B} = \partial\mathbf{N}$. $\mathbf{p}$ is surface pressure term, and $\mathbf{b}$ is body force.

Sensitivity equations

Sensitivity analysis is one of the important aspects in engineering design theory and application. The expressions of eigenvalue sensitivity and eigenvector sensitivity are computed by deriving the first order sensitivities for symmetric positive definite eigenvalue systems (13). The equations are given by D. A. Tortorelli and P. Michaleris [27]:

$$\frac{D\lambda_j}{Dd_i} = \phi_j^0 \cdot \left[\frac{D\mathbf{K}}{Dd_i} - \lambda_j \frac{D\mathbf{K}_s}{Dd_i}\right]\phi_j^0 \tag{16}$$

19

where ϕ_j^0 is the normalized eigenvectors of ϕ_j, and $\mathbf{d}$ is design parameter vector.

The derivative of eigenvectors are given by the equation:

$$[\mathbf{K} - \lambda_j \mathbf{K}_s] \frac{D\phi_j}{Dd_i} = - \left[\frac{D\mathbf{K}}{Dd_i} - \lambda_j \frac{D\mathbf{K}_s}{Dd_i} \right] \phi_j - \frac{D\lambda_j}{Dx_i} \mathbf{K}_s \phi_j \qquad (17)$$

Noticing $[\mathbf{K} - \lambda_j \mathbf{K}_s]$ is singular now, first assume the s-th component $\phi_{js} \equiv 1$, thus $\frac{D\phi_{js}}{Dx_i} \equiv 0$, remove the corresponding row and column in $[\mathbf{K} - \lambda_j(x)\mathbf{K}_s]$, then comes a equation from which other components of $\frac{D\phi_j}{Dx_i}$ can be solved.

3.2.2 Numerical implementation and verification

The buckling and sensitivity equations has been integrated into FORTRAN code, and used in the following numerical examples. Results are presented here for two simple examples. The analytical solution along with results obtained using the commercial code ABAQUS are presented for verification.
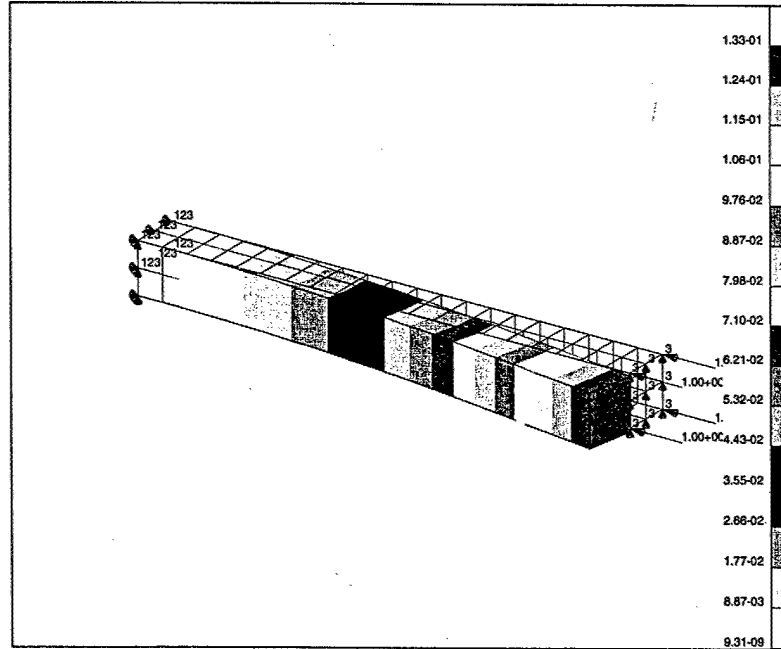
Model information

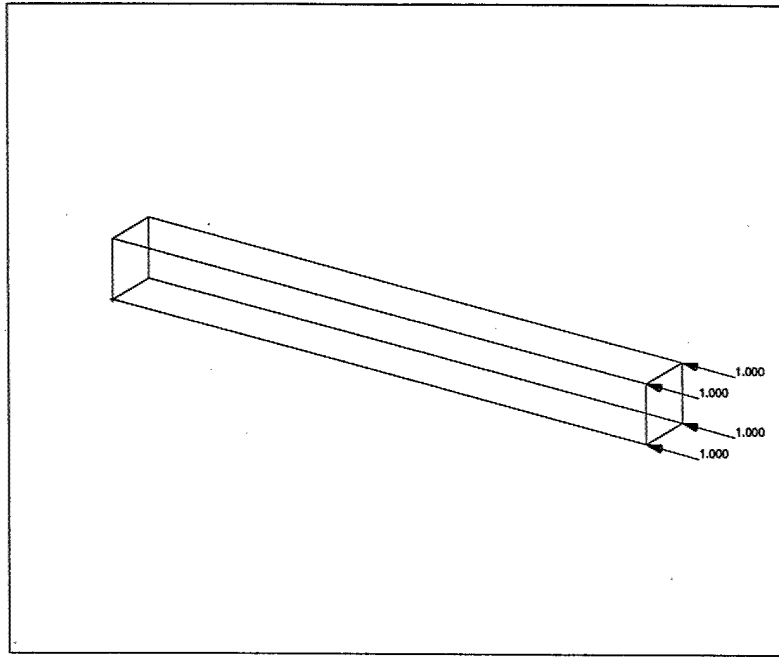Figure 17: cantilever beam, 1st buckling mode

Figure 18: load information

The first example is a cantilever beam, all three degrees of freedom for the nodes at one end and one vertical degree of freedom for nodes at the other end are constrained. A unit surface pressure is applied at the latter surface as load. Please, refer to Figure 17 for the model information and Figure 18 for the load information.

The second example is a simple supported beam, where at the fixed end all three degrees of freedom are constrained and a unit surface pressure is applied at the other end. See Figure 19 for the model information. The load information is the same as the first one.

The length, width and height of both beams are 10, 1, 1 respectively, with Young's modula $E = 2.0E5$ and Poisson's ratio $\gamma = 0$.

Results and comparison

Table 3.2.2 presents a comparison of the eigenvalues for the two example problems. Analytical results, computational results using the commercial code ABAQUS and the in-house FORTRAN code are listed. Table 3.2.2 presents a comparison of the sensitivities of eigenvalues with respect to the beam length for the two example problems. Analytical results, computational results using the direct differentiation and finite difference of the in-house FORTRAN code are listed.

For the cantilever beam, the approximate theoretical critical buckling load can be expressed as: $P_{cr} = \frac{\pi^2 EI}{4L^2} = 411.23$, where $\phi = \phi_c sin(\frac{\pi x}{2L})$ is used as the approximate buckling mode. The result from ABAQUS is $P_{cr} = -889.21$, and from the FORTRAN code is $P_{cr} = 460.04$. The buckling
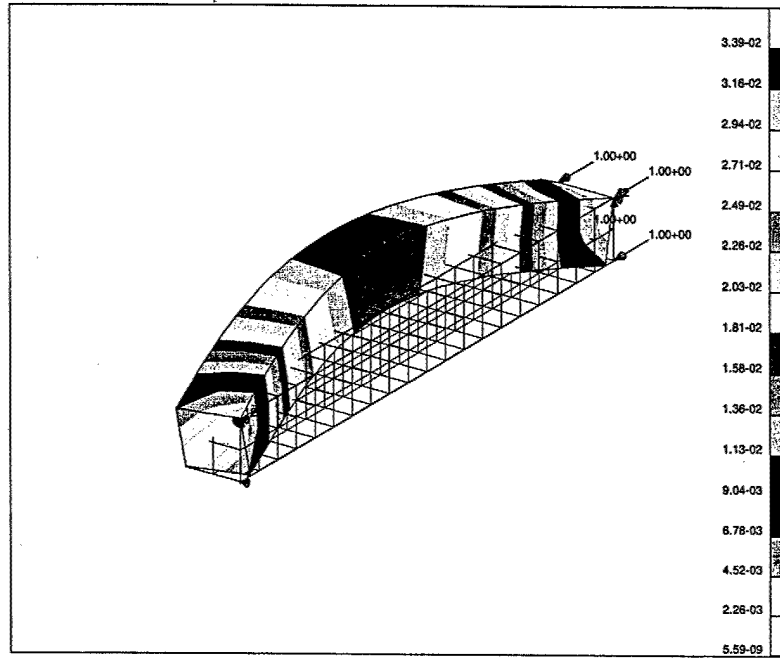
Figure 19: simple supported beam, 1st buckling mode

modes are same from ABAQUS and the FORTRAN code, as in Figure 17.

The sensitivity of the eigenvalue with respect to the length of the beam as calculated from FORTRAN code using Equation (16) is $\Delta P = -80.3$. To verify this result, the sensitivity is also computed by the finite difference method. The length of beam is changed to 10.1, with other properties remaining the same, the critical buckling load changes to $P_{cr} = 452.04$ which results to a finite difference sensitivity of 80.0.

For the simply supported beam, the approximate theoretical critical buckling load is $P_{cr} = \frac{\pi^2 EI}{L^2} = 1644.93$, where $\phi = \phi_c sin(\frac{\pi x}{L})$ is used as approximate buckling mode. The result from ABAQUS is $P_{cr} = 1633.7$, and from FORTRAN code is $P_{cr} = 1688.81$. The result of buckling modes are also same from ABAQUS and FORTRAN code, as in Figure 19.

For the finite difference sensitivity, the critical buckling load for the beam with length 10.1 is $P_{cr} = 1661.58$ which results to the finite difference sensitivity of $\Delta P = -272.3$. The numerical sensitivity result calculated from FORTRAN code is $\Delta P = -272.8$.

model	Analytical method	ABAQUS	FORTRAN code
1	411.23	-889.21	460.04
2	1644.93	1633.7	1688.81

Table 5: Eigenvalues calculated from analytical method, ABAQUS and FORTRAN code

model	Analytical method	Finite difference method	FORTRAN code
1	-82.2	-80.0	-80.3
2	-329.0	-272.3	-272.8

Table 6: Sensitivities calculated from analytical method, finite difference and FORTRAN code

3.3 Generation of a database

Work in this task will commence in FY 02.

3.4 Integration with computer aided production engineering software

Work in this task will commence in FY 02.

3.5 Modifications and refinement using production tests

Work in this task will commence in FY 02.

References

[1] K. Masubuchi. *Analysis of Welded Structures*. Pergamon Press, Oxford, 1980.

[2] A. P. Chakravati, L. M. Malik, and J. A. Goldak. Prediction of Distortion and Residual Stresses in Panel Welds. In *Computer modelling of fabrication processess and constitutive behaviour of metals*, pages 547–561, Ottawa, Ontario, 1986.

[3] J. Goldak and M. Bibby. Computational Thermal Analysis of Welds: Current Status and Future Directions. In A. F. Giamei and G. J. Abbaschian, editors, *Modeling of Casting and Weldin Processes IV*, pages 153–166, Palm Coast, FL, 1988. The Minerals & Materials Society.

[4] H. Hibbitt and P. V. Marcal. A Numerical, Thermo-Mechanical Model for the Welding and Subsequent Loading of a Fabricated Structure. *Computers & Structures*, 3(1145-1174):1145–1174, 1973.

[5] J. H. Argyris, J. Szimmat, and K. J. Willam. Computational Aspects of Welding Stress Analysis. *Computer Methods in Applied Mechanics and Engineering*, 33:635–666, 1982.

[6] E. F. Rybicki, D. W. Schmueser, R. B. Stonesifer, J. J. Groom, and H. W. Mishler. A Finite-Element Model for Residual Stresses and Deflections in Girth-Butt Welded Pipes. *Journal of Pressure Vessel Technology*, 100:256–262, 1978.

[7] V.J Papazoglou and K. Masubuchi. Numerical Analysis of Thermal Stresses during Welding including Phase Transformation Effects. *Journal of Pressure Vessel Technology*, 104:198–203, 1982.

[8] Y. Ueda KH. Murakawa N. X. Ma and H. Maeda. FEM Analysis of 3-D Welding Residual Stresses and Angular Distortion in T-type Fillet Welds. *Transactions of JWRI*, 24(2):115–122, 1995.

[9] S.B. Brown and H. Song. Implications of Three-Dimensional Numerical Simulations of Welding of Large Structures. *Welding Journal*, 71(2):55s–62s, 1992.

[10] P. Michaleris, Z. Feng, and G. Campbell. Evaluation of 2D and 3D FEA Models for Predicting Residual Stress and Distortion. In *Pressure Vessel and Piping Conference*. ASME, 1997.

[11] A. S. Oddy, J. A. Goldak, and J. M. J. McDill. Numerical Analysis of Transformation Plasticity in 3 D Finite Element Analysis of Welds. *European Journal of Mechanics, A/Solids*, 9(3):253–263, 1990.

[12] P. Tekriwal and J. Mazumder. Finite Element Analysis of Three-dimensional Tranient Heat Transfer in GMA Welding. *A.W.S. Welding Journal, Research Supplement*, 67:150s–156s, 1988.

[13] P. Tekriwal and J. Mazumder. Transient and Residual Thermal Strain-Stress Analysis of GMAW. *Journal of Engineering Materials and Technology*, 113:336–343, 1991.

[14] Y. Yeda and H. Murakawa. Applications of Computer and Numerical Analysis Techniques in Welding Research. *Transactions of JWRI*, 13(2):165–174, 1984.

[15] E. F. Rybicki and R. B. Stonesifer. Computation of Residual Stresses due to Multipass Welds in Piping Systems. *Journal of Pressure Vessel Technology*, 101:149–154, 1979.

[16] H. Murakawa Y. Ueda X. M. Zhong. Buckling Behavior of Plates under Idealized Inherent Strain. *Transactions of JWRI*, 24(2):87–91, 1995.

[17] P. Michaleris and A. DeBiccari. Prediction of Welding Distortion. *Welding Journal*, 76(4):172–180, 1997.

[18] C.L. Tsai, S.C. Park, and W.T. Cheng. Welding Distortion of a Thin-Plate Panel Structure. *A.W.S. Welding Journal, Research Supplement*, 78:156s–165s, 1999.

[19] Y. Ueda, Y.C Kim, and M.G Yuan. A Predictive Method of Welding Residual Stress Using Source of Residual Stress (Report I) Characteristics of Inherent Strain (Source of Residual Stress). *Transactions of JWRI*, 18(1):135–141, 1989.

[20] P. Michaleris and A. DeBiccari. A Predictive Technique for Buckling Analysis of Thin Section Panels due to Welding. *Journal of Ship Production*, 12(4):269–275, 1996.

[21] D.F.Watt, L.Coon, M.Bibby, and C.Henwood. An algorithm for modeling microstructural development in weld heat affected zones (part a) reaction kinetics. *Acta metall.*, 36(11):3029–3035, 1988.

[22] J.B LeBlond and J.Devaux. A new kinetic model for anisothermal metallurgical transformations in steels including effect of austenite grain size. *Acta metall.*, 32(1):137–146, 1984.

[23] D.F.Watt, L.Coon, M.Bibby, and C.Henwood. Coupled transient heat transfer-microstructure weld computations (part b). *Acta metall.*, 36(11):3037–3046, 1988.

[24] J. Goldak, A. Chakravarti, and M. Bibby. A New Finite Element Model for Welding Heat Sources. *Metallurgical Transactions B*, 15B:299–305, 1984.

[25] K. J. Bathe. *Finite Element Procedures in Engineering Analysis*. Prentice-Hall, Inc., Englewood Cliffs, New Jersey, NJ, 1982.

[26] H.K.S. *ABAQUS Theory Manual*. H.K.S, 1998.

[27] D. A. Tortorelli and P. Michaleris. Design Sensitivity Analysis: Overview and Review. *Inverse Problems in Engineering*, 1:71–103, 1994.